

The Role of Intrinsic Temperature and Vertical Mixing in Characterizing Sub-Neptune Atmospheres.

NEHA DUSHYANTHA KUMAR,^{1,2} JESSICA E. LIBBY-ROBERTS,^{1,2,3} CALEB I. CAÑAS,^{4,5} NICHOLAS F. WOGAN,^{6,7} SUVRATH MAHADEVAN,^{1,2} AND SAGNICK MUKHERJEE⁸

¹Department of Astronomy & Astrophysics, 525 Davey Laboratory, The Pennsylvania State University, University Park, PA 16802, USA

²Center for Exoplanets and Habitable Worlds, The Pennsylvania State University, University Park, PA 16802, USA

³Department of Physics and Astronomy, University of Tampa, Tampa, FL 34606, USA

⁴Southeastern Universities Research Association, Washington, DC 20005, USA

⁵NASA Goddard Space Flight Center, 8800 Greenbelt Road, Greenbelt, MD 20771, USA

⁶Space Science Division, NASA Ames Research Center, Moffett Field, CA 94035, USA

⁷Virtual Planetary Laboratory, University of Washington, Seattle, WA 98195, USA

⁸School of Earth and Space Exploration, Arizona State University, Tempe, AZ 85287, USA

ABSTRACT

Sub-Neptune planets are often modeled with a dense rocky or metal-rich interior beneath a thick hydrogen/helium (H/He) atmosphere; though their bulk densities could also be explained by a water-rich interior with a thin H/He atmosphere. Atmospheric composition provides a key mechanism to break this degeneracy between competing interior models. However, the overall composition of sub-Neptunes inferred from spectra obtained with the James Webb Space Telescope, remains debated in part due to differences in modeling assumptions. While previous studies explored parameter spaces such as stellar spectra, atmospheric metallicities, and carbon-to-oxygen ratios, they often assumed fixed intrinsic temperatures (T_{int}) and vertical eddy diffusion coefficients (K_{zz}) - two critical, yet poorly constrained, drivers of atmospheric chemistry. To address this, we present a self-consistent grid of models that covers the full plausible range of T_{int} (60 - 450 K) and K_{zz} (10^5 - 10^{12} cm²/s) using the open-source PICASO and VULCAN packages to better characterize sub-Neptune atmospheres. Focusing on K2-18b analogs, we demonstrate that T_{int} and K_{zz} significantly impact CH₄, CO₂, CO, NH₃ and HCN abundances, with H₂O being largely unaffected. Our work demonstrates that comprehensive parameter space exploration of thermal and mixing parameters is essential for accurate interpretation of sub-Neptune spectra, and that single-parameter assumptions can lead to misclassification of planetary interiors. We provide a diagnostic framework using multi-molecule observations to distinguish between competing atmospheric models and advance robust characterization of sub-Neptunes.

Keywords: Exoplanet atmospheres (487) – Exoplanet atmospheric composition (2021) – Mini Neptunes (1063) – Transmission spectroscopy (2133) – Theoretical models (2107)

1. INTRODUCTION

Sub-Neptunes, exoplanets with radii between 1.6 and $3.2 R_{\oplus}$ (e.g. L. A. Rogers 2015; A. Wolfgang et al. 2016; B. J. Fulton et al. 2017) are one of the most common planet populations discovered so far (e.g. B. J. Fulton & E. A. Petigura 2018; D. C. Hsu et al. 2019). Without sub-Neptune analogs in our own Solar System, we must rely on bulk densities to inform our understanding of their interior compositions. One explanation of their bulk densities is a smaller, denser interior beneath a thick hydrogen/helium (H/He) envelope (L. A. Rogers & S. Seager 2010a,b; B. Benneke & S. Seager 2013). However, their bulk densities of $1\text{--}3$ g cm⁻³ (compared to Earth's 5.5 g cm⁻³) can also be explained by interiors comprised of deep, global water oceans beneath a thin H/He atmosphere, often denoted as

Hycean worlds (N. Madhusudhan et al. 2021). Alternatively, these densities can be accounted for by soot planets, which incorporate refractory organic carbon (referred to as soot) as a major component (J. Li et al. 2025). Sub-Neptunes, specifically Hycean worlds (N. Madhusudhan et al. 2021), are a subject of detailed habitability studies (e.g. N. Madhusudhan et al. 2023; H. Innes et al. 2023; E. G. Mitchell & N. Madhusudhan 2025). We can break the degeneracy in a planet's bulk density by characterizing their fundamental differences which lie in their atmospheric composition (e.g., N. Madhusudhan et al. 2021; X. Yu et al. 2021; S.-M. Tsai et al. 2021; B. Benneke et al. 2024; N. F. Wogan et al. 2024; G. J. Cooke & N. Madhusudhan 2024; J. Li et al. 2025).

Exoplanet atmospheric characterization primarily uses transmission and emission spectroscopy, with missions like the James Webb Space Telescope (JWST) (J. P. Gardner et al. 2006) enabling new levels of precision (N. Espinoza & M. D. Perrin 2025; J. de Wit et al. 2025). However, interpretation of these observations require atmospheric models, which broadly fall into two categories: self-consistent forward modeling and retrievals (N. Madhusudhan & S. Seager 2009; A. R. Howe et al. 2017).

Self-consistent forward modeling involves constructing atmospheric models based on a realistic combination of underlying physical and chemical processes (e.g., radiative-convective equilibrium, thermochemical equilibrium, photochemistry) that self-consistently predict temperature-pressure profiles, chemical abundances, and synthetic spectra from first principles, which can then be directly compared to observations using various statistical metrics (N. Madhusudhan & S. Seager 2009; A. R. Howe et al. 2017). Retrievals, by contrast, statistically invert observed spectra to directly infer atmospheric parameters, offering flexibility to explore regions of parameter space not constrained by forward model assumptions (with the danger that some solutions may be nonphysical). This approach, therefore, can yield more comprehensive uncertainty estimates and identify potential model inadequacies (L. Kreidberg 2018).

Atmospheric dynamics is complex (L. D. Deming & S. Seager 2017; M. Roman & E. Rauscher 2019; M. E. Steinrueck et al. 2023), dependent on both planetary and stellar factors. Key model influences include large scale inputs such as stellar irradiation (J. J. Fortney 2018) and planetary masses, radii, and equilibrium temperatures, down to the smaller scale processes of chemical reactions (C. Visscher et al. 2010; J. I. Moses et al. 2011), 3D atmospheric dynamics, and molecular line lists (M. S. Marley et al. 2021). Because these factors are complex and at times not well-constrained, interpretations of exoplanet atmospheric models are highly sensitive to the choice of underlying assumptions (J. K. Barstow et al. 2017).

Metallicity, carbon-to-oxygen (C/O) ratios and stellar luminosity (in the Ultraviolet) driven photochemistry have been the dominant parameters explored in sub-Neptune atmospheric models (O. Shorttle et al. 2024; R. Hu et al. 2025; A. Y. Jaziri et al. 2025; S. Mukherjee et al. 2025; I. J. M. Crossfield et al. 2025). X. Yu et al. (2021) extended the parameter space to explore the impacts of shallow versus deep surfaces. However, the majority of these studies assume a constant intrinsic temperature (T_{int}) and vertical mixing coefficient (K_{zz}) throughout the model grid; values that, although based on educated guesses, remain poorly constrained by observations. Carbon, oxygen and nitrogen-bearing species are central to atmospheric models because they drive disequilibrium chemistry via quenching, thus determining the deep atmosphere quench point that controls the observable abundances of key molecules like CH₄ and CO (M. Zamyatina et al. 2024). Recent JWST observations of the warm-Neptune, WASP-107b (D. K. Sing et al. 2024; L. Welbanks et al. 2024), demonstrate that vigorous K_{zz} and a hot intrinsic temperature T_{int} are required to explain order-of-magnitude CH₄ depletion and CO enhancement. Similarly, disequilibrium retrievals highlight the sensitivity of species like NH₃ to vertical transport and interior heat (V. Soni & K. Acharyya 2024; R. Hu et al. 2025).

Moreover, photochemical recycling in sub-Neptune atmospheres depends critically on both interior temperature and surface depth. In deep, surface-less envelopes, CH₄ and NH₃ produced in the upper atmosphere can be carried downward, converted back to equilibrium species in hot layers, and then mixed upward again, preserving their abundances against photolytic loss. By contrast, a shallow surface (≤ 10 bar) cuts off this recycling: CH₄ and NH₃ are destroyed by stellar UV and cannot be replenished, shifting the chemistry toward CO, CO₂, and N₂ dominance (X. Yu et al. 2021). Thus, both hot interiors and shallow surfaces produce low CH₄ but through different mechanisms. Water condensation at the lower boundary further depletes oxygen-bearing molecules, raising the C/O ratio and promoting higher-order hydrocarbons and organic hazes (Z. Huang et al. 2024), though existing chemical networks may underestimate destruction of complex organics (S.-M. Tsai et al. 2021).

A significant limitation in previous investigations is that models used to interpret disequilibrium chemistry rely on simplified pressure-temperature (P - T) profiles. This leads to atmospheric chemistry not being fully self-consistent with

radiative-convective transport. To expand on earlier work, we systematically explore the previously under constrained parameter space of intrinsic temperature and vertical mixing to characterize their influence on sub-Neptune atmospheric composition and observability. We create a set of model grids that couple hot interior structure with quench driven chemistry for a K2-18b sub-Neptune analog using the radiative-convective code **PICASO** (N. E. Batalha et al. 2019; N. Batalha et al. 2022; S. Mukherjee et al. 2023) and the photochemical code **VULCAN** (S.-M. Tsai et al. 2021) (Section 2). Our model grid explores T_{int} ranging from 60–450 K and K_{zz} covering 10^5 - 10^{12} cm²/s, along with the variable K_{zz} profile specified in R. Hu (2021); N. F. Wogan et al. (2024), thus spanning the full range of plausible, yet unexplored, mixing and thermal states. For each case, we compute transmission spectra from 0.6–5 μ m, analyzing CH₄, CO, CO₂, and NH₃ features.

From this comprehensive parameter space exploration, we present our key results in Section 3 by examining molecular abundance patterns that reveal distinct sensitivity regimes for different species (Subsection 3.1), vertical abundance profiles that demonstrate quenching behavior across temperature and mixing conditions (Subsection 3.2), and transmission spectra that show systematic spectral evolution reproducing observed K2-18b features (Subsection 3.3). In Section 4, we discuss the implications our results have on the current population of sub-Neptunes, and we conclude in Section 5 by summarizing our diagnostic framework for distinguishing between competing atmospheric scenarios and its broader applications to temperate sub-Neptune characterization with current and future observatories.

2. METHODS

2.1. Target Selection: K2-18b Analog

In this work, we define K2-18b analogs as temperate sub-Neptunes with radii, masses, and equilibrium temperatures similar to K2-18b (Table 1), where both Hycean world and gas-rich sub-Neptune interpretations remain plausible. K2-18b (B. T. Montet et al. 2015), with its well-constrained radius and mass ($2.610 \pm 0.087, R_{\oplus}$, $8.63 \pm 1.35, M_{\oplus}$, respectively; B. Benneke et al. 2019), serves as an ideal test case to distinguish how interior heat and mixing influence the observed spectra. Existing atmospheric analyses span a wide range of proposed compositions, from water-rich Hycean worlds with relatively thin H/He atmospheres (N. Madhusudhan et al. 2021, 2023; R. Hu et al. 2025) to gas-rich sub-Neptunes with thick hydrogen envelopes (N. F. Wogan et al. 2024; O. Shortle et al. 2024; N. Madhusudhan et al. 2020; B. Benneke et al. 2019). Independent reanalyses and joint retrievals have demonstrated that key inferences, such as CO₂ strength and the presence of sulfur species, can be sensitive to data reduction and modeling assumptions (G. J. Cooke & N. Madhusudhan 2024).

These ongoing investigations of K2-18b have revealed the complexity of distinguishing between different atmospheric scenarios for sub-Neptune planets, motivating us to explore additional regions of parameter space that have been previously under-explored. By systematically varying the intrinsic temperature and vertical mixing - parameters typically held fixed in earlier modeling efforts - we aim to understand how these critical drivers influence atmospheric chemistry and observable signatures in K2-18b analogs. We compare our model grid predictions with existing atmospheric models for K2-18b, particularly the sub-Neptune framework developed by N. F. Wogan et al. (2024), to validate our approach and demonstrate how thermal and mixing parameters affect molecular abundance patterns. This comprehensive parameter space exploration will enable future studies to better disentangle the complexities of sub-Neptune atmospheric composition by providing a systematic framework for understanding how interior thermal structure and vertical transport processes control observable spectral features across the broader population of temperate sub-Neptunes.

We built our model grid using the stellar and planetary parameters in Table 1. To emphasize, our modeling framework and conclusions are directly applicable to other temperate sub-Neptunes (equilibrium temperatures 250–300 K) with similar mass–radius characteristics, which we term **K2-18b analogs**. Figure 1 showcases the current population of sub-Neptunes with known masses and radii. Potential Hycean-worlds adapted from the list supplied in N. Madhusudhan et al. (2021) are highlighted within the broader sub-Neptune population, falling within the transition region between super-Earths and sub-Neptunes where both rocky, gas-rich, water-rich compositions remain plausible (X. Yu et al. 2021).

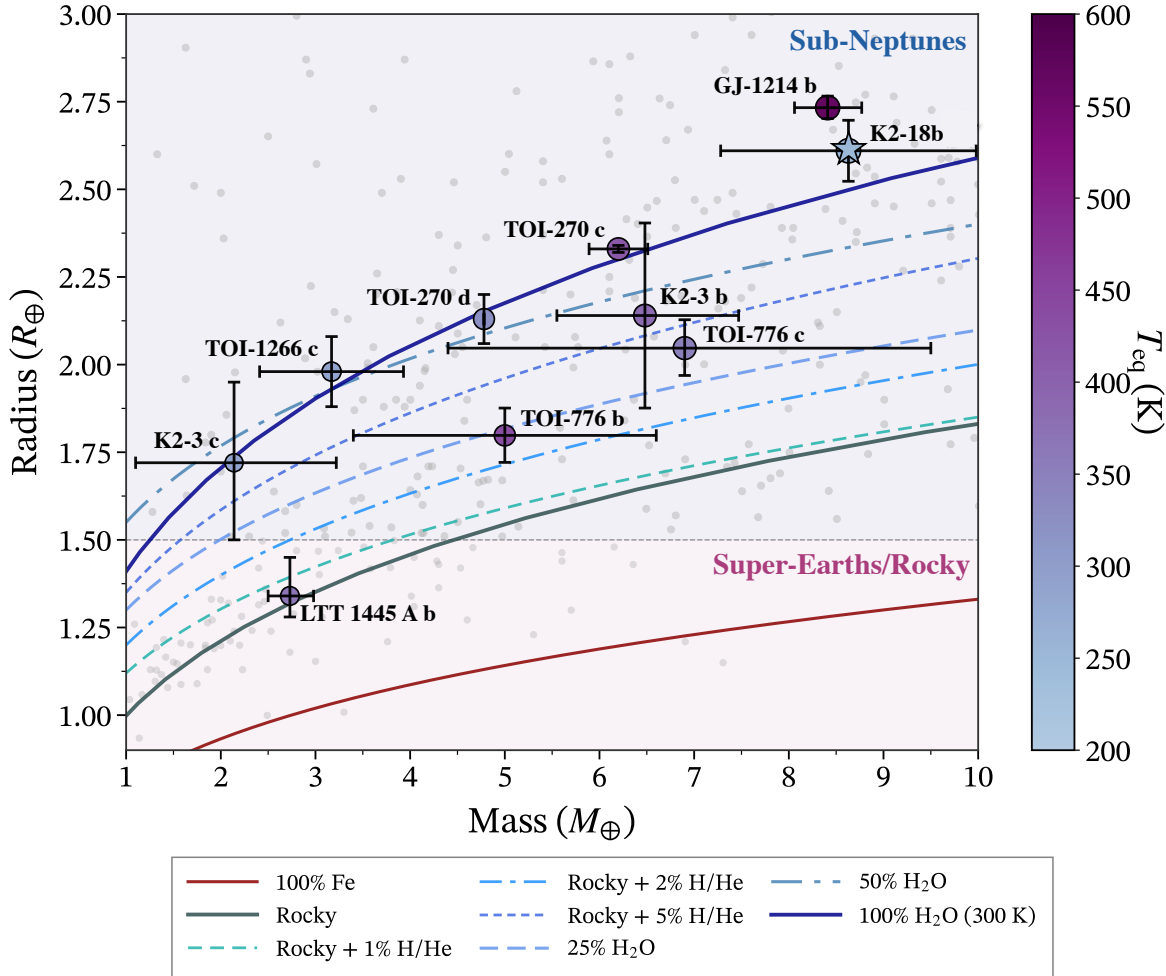


Figure 1. Transiting exoplanets with measured masses and radii from the *exoatlas Transiting Exoplanets* catalog (Z. K. Berta-Thompson et al. 2025). The gray points represent the sub-neptune population extracted from *exoatlas*. The selected possible Hycean worlds from N. Madhusudhan et al. (2021) are labeled with error bars for reference; point color encodes equilibrium temperature (K) ranging from 200 K to 600 K using values taken from the NASA Exoplanet Archive (J. L. Christiansen et al. 2025) assuming zero albedo. K2-18b analogs – sub-Neptunes with comparable bulk properties and equilibrium temperatures (250–300 K) that occupy the compositional transition region where both Hycean world and gas-rich sub-Neptune interpretations remain plausible, are highlighted within this population. The regime boundaries between super-Earth/rocky composition (light purple) and sub-Neptune/gas-rich (blue) are based on the radius criterion of $1.6R_{\oplus}$ from L. A. Rogers (2015), with sub-Neptunes defined as planets with radii between 1.6 and $3.2R_{\oplus}$. Solid and dashed composition curves from L. Zeng & S. Seager (2008); L. Zeng et al. (2019) for rocky and hydrogen-rich planets showcase the degeneracy in mass-radius space. Shaded regions are not strict classifications.

2.2. PICASO: Climate Modeling with Equilibrium Chemistry

We used **PICASO** v3.0 (N. E. Batalha et al. 2019; N. Batalha et al. 2022; S. Mukherjee et al. 2023) to generate self-consistent pressure-temperature (P-T) profiles and equilibrium chemical abundances for K2-18b-like atmospheres. For each model, we configured **PICASO** to assume a 1-Dimensional, clear-sky atmosphere under thermochemical equilibrium conditions, neglecting photochemistry and vertical mixing processes that are handled separately by **VULCAN** (Section 2.3).

We initialized each **PICASO** simulation with the planetary and stellar parameters in Table 1, assuming a $100\times$ solar metallicity atmosphere and a solar C/O ratio (~ 0.5). Given K2-18's M dwarf classification and effective temperature,

Table 1. Fixed model planetary and stellar parameters based on K2-18 system

Category	Parameter	Value	Source
Planetary	Planet Mass (M_p)	$8.63 \pm 1.35 M_\oplus$	B. Benneke et al. (2019)
	Planet Radius (R_p)	$2.610 \pm 0.087 R_\oplus$	B. Benneke et al. (2019)
	Equilibrium Temperature (T_{eq})	254 ± 3.9 K	B. Benneke et al. (2019)
	Planet Bulk Density (ρ_p)	$2.67^{+0.52}_{-0.47}$ g/cm ³	B. Benneke et al. (2019)
	Surface Gravity (g_p)	1234.85 cm/s ²	B. Benneke et al. (2019)
Stellar	Stellar Mass (M_*)	$0.4951 \pm 0.0043 R_\odot$	B. Benneke et al. (2019)
	Stellar Radius (R_*)	$0.4445 \pm 0.0148 R_\odot$	B. Benneke et al. (2019)
	Effective Temperature (T_{eff})	3457 ± 39 K	B. Benneke et al. (2019)
	Metallicity ([Fe/H])	$+0.12 \pm 0.16$ dex	P. Sarkis et al. (2018)
	Surface Gravity ($\log g_*$)	4.786 ± 0.006	K. G. Stassun et al. (2019)

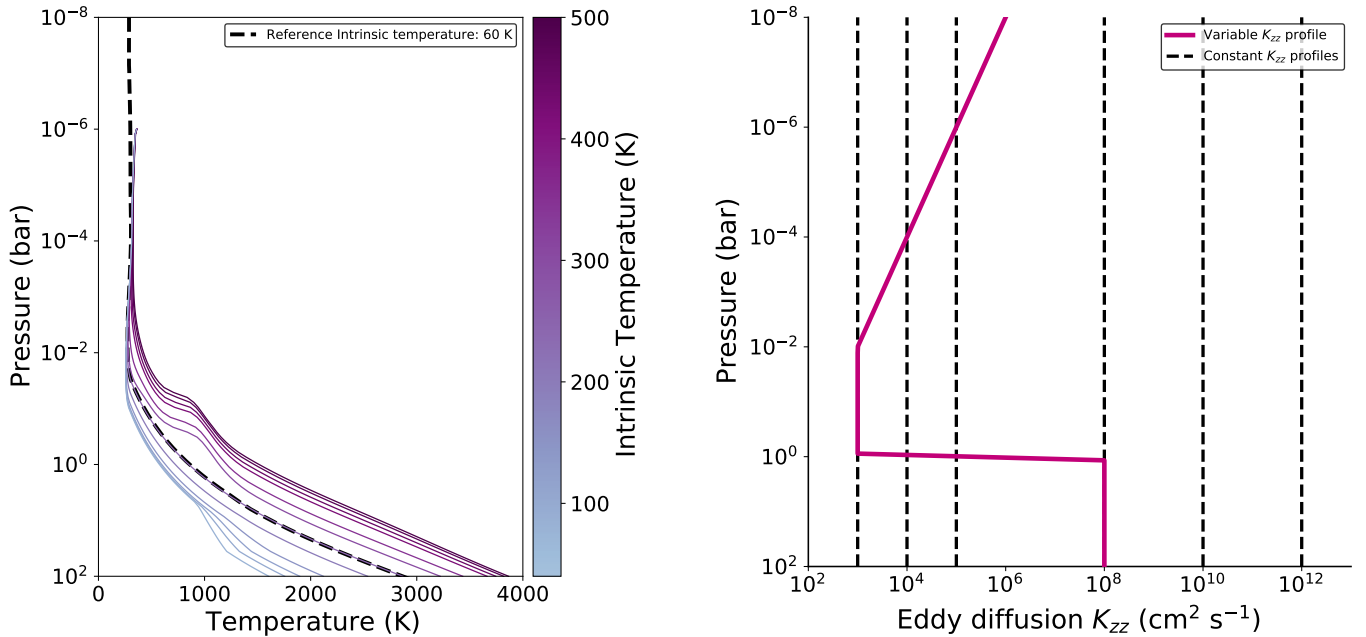


Figure 2. **Left:** Pressure-temperature profiles for a K2-18b-like atmosphere generated by PICASO across varying intrinsic temperatures (T_{int}) from 60 to 450 K. The color gradient represents different T_{int} values, with cooler interiors in blue and hotter interiors in purple. The dashed black line shows the reference case with $T_{int} = 60$ K, which has been commonly adopted in previous atmospheric models of K2-18b. The curvature around 0.1 bar shown in Figure 2 is expected in these PT profiles because that is where the incident stellar irradiation is absorbed by atmospheric gases. **Right:** Pressure-dependent eddy diffusion coefficient (K_{zz}) profile for a sub-Neptune model of K2-18b with $100\times$ solar metallicity. The purple line shows the model K_{zz} profile used in this study, which follows a Jupiter-like eddy diffusion profile in the upper atmosphere (1 bar to 10^{-8} bar) as adopted from R. Hu (2021); N. F. Wogan et al. (2024). The deep atmosphere (500 bar to 1 bar) uses constant K_{zz} values from 10^5 - 10^{12} cm^2/s . Black dashed vertical lines indicate the range of constant K_{zz} values used in our model grid.

we employed PHOENIX stellar atmosphere models (T.-O. Husser et al. 2013). These values are consistent with JWST observations, particularly for K2-18b (N. Madhusudhan et al. 2023; N. F. Wogan et al. 2024; A. Y. Jaziri et al. 2025). The atmospheric grid spans 91 pressure levels spaced from 10^2 to 10^{-6} bar, with molecular opacities from the correlated- k opacity database of R. Lupu et al. (2021). We used T. Guillot (2010) pressure-temperature parameterization as the initial P-T profile and set the heat redistribution factor to $r_{\text{facv}} = 0.5$ to represent day-night heat transport (e.g., a planet-wide average P-T profile). The relatively large orbital distance ($a/R_* = 48.7$; B. Benneke et al. 2019) indicates

K2-18b likely experiences efficient day-night heat redistribution through atmospheric circulation, unlike the inefficient transport in tidally locked systems (J. Leconte et al. 2015).

Our climate and equilibrium chemistry calculations included a H/He-dominated atmosphere, major molecular species (H_2O , CO , CO_2 , CH_4 , NH_3 , HCN , C_2H_2 , C_2H_4), trace gases (NO , OH , CN , PH_3), atomic species (Na, K, Fe), ions (H^+ , H^- , e^-), and collision-induced absorption from H_2 - H_2 and H_2 -He pairs (R. Lupu et al. 2021). PICASO accounts for refractory species which condense at K2-18b's equilibrium temperature of 250 K and are thus removed from the gas phase in the deep atmosphere.

To explore the impact of interior heating on atmospheric structure, we systematically varied the intrinsic temperature (T_{int}) from 60 K to 450 K at the discrete values 60, 100, 150, 200, 250, 300, 350, 400 and 450 K. The intrinsic temperature parameterizes the internal heat flux from the planet's interior and is related to the effective temperature through

$$T_{\text{eff}}^4 = T_{\text{eq}}^4 + T_{\text{int}}^4, \quad (1)$$

where $T_{\text{eq}} = 254$ K is the equilibrium temperature of K2-18b (B. Benneke et al. 2019) and T_{eff} is the total effective temperature driving the atmospheric thermal structure (T. Guillot 2010; J. J. Fortney et al. 2020). The intrinsic luminosity is given by

$$L_{\text{int}} = 4\pi R_p^2 \sigma T_{\text{int}}^4, \quad (2)$$

where R_p is the planetary radius and σ is the Stefan-Boltzmann constant. For each T_{int} value, we computed radiative-convective equilibrium by iteratively adjusting the pressure-temperature profile until energy balance was achieved within a 0.1% tolerance. We initially attempted to include models with $T_{\text{int}} = 40$ K to extend our parameter space to even cooler interior conditions. However, these models failed to achieve stable radiative convective equilibrium within our convergence tolerance, exhibiting persistent oscillations in the deep atmospheric thermal structure. Since disequilibrium chemistry is fundamentally determined by the deep thermal structure and quench point locations, unconverged pressure-temperature (P-T) profiles would introduce systematic errors in the photospheric chemical abundances that form the basis of our transmission spectra analysis. We therefore excluded $T_{\text{int}} = 40$ K from our final model grid to ensure that all chemical trends reported are based on properly converged atmospheric structures. Figure 2 shows the resulting pressure-temperature (P-T) profiles for a planet similar in structure to K2-18b across this range of intrinsic temperatures, illustrating how increased internal heating systematically raises temperatures throughout the deep atmosphere while leaving the upper atmosphere largely unchanged.

For the upper atmosphere, the P-T profile was adapted to become isothermal following the framework in N. F. Wogan et al. (2024). The isothermal temperature was set to the equilibrium temperature of 250 K at the 10 mbar level from the converged radiative convective profile. These outputs served as initial conditions for the subsequent VULCAN disequilibrium chemistry calculations. The curvature around 0.1 bar shown in Figure 2 is expected in these PT profiles because that is where the incident stellar irradiation is absorbed by atmospheric gases.

2.3. VULCAN: Disequilibrium and Photochemistry

We used VULCAN (S.-M. Tsai et al. 2021) to compute disequilibrium chemical abundances, taking the P-T profiles generated by PICASO (see Section 2.2) as input and evolving the atmospheric chemistry beyond thermochemical equilibrium. For each PICASO model, we configured VULCAN to include photochemistry, vertical mixing, and condensation processes for H_2O that are essential to simulate the atmospheric conditions of planets like K2-18b.

Our atmosphere was configured as H/He-dominated to reflect a gas-rich envelope. We again used 91 vertical layers, spanning a wide pressure range from a bottom pressure $P_b = 10^3$ bar to a top pressure $P_t = 10^{-8}$ bar, to capture the full vertical extent of the observable atmosphere similar to Section 2.2. To account for vertical transport, we enabled both eddy and molecular diffusion. We specified a range of constant eddy diffusion coefficients for the Constant K_{zz} Profile from 10^5 - 10^{12} cm^2/s to systematically explore the effects of vertical mixing on the atmospheric chemistry and followed the K_{zz} profile from (N. F. Wogan et al. 2024) for the Variable K_{zz} Profile. Large scale vertical advection was disabled to isolate the influence of other transport mechanisms.

We implemented the NCHO chemical network containing around 100 NCHO species with thermodynamically consistent reversible reactions. We adopted a customized set of elemental abundances, specifically assuming 100× solar metallicity and a solar C/O ratio. This choice was motivated by prior modeling from N. F. Wogan et al.

(2024), which showed that volatile enriched atmospheres can reproduce the inferred composition of K2-18b, including strong CO₂ and CH₄ features and the absence of NH₃. We also included sulfur chemistry in our initial configuration, but did not include the full SNCHO network in our model grids for computational simplicity. While sulfur photochemistry can produce various sulfur-bearing species under disequilibrium conditions, we focused on the NCHO network to isolate the effects of intrinsic temperature and vertical mixing on the primary carbon, nitrogen, and oxygen chemistry that drives our spectral diagnostics. We verified this approach by running a benchmark SNCHO test, which showed a difference of 1.8 ppm compared to our NCHO models.

To verify that the predicted composition remained effectively unchanged when sulfur chemistry is included, we ran an SNCHO test for a benchmark case adopting the variable K_{zz} profile and $T_{int} = 60$ K. A comparison of the resulting transmission spectra over 0.6–5.3 μm (Section 2.4) yields wavelength-averaged differences of 1.2 ± 0.5 ppm between the NCHO and SNCHO models (Figure A1). The largest difference occurred in the CO₂ absorption region near 4.3 μm (≤ 7 ppm) and in the CO feature at 4.6 μm (4 ppm), while CH₄ diagnostic features at 2.3 and 3.3 μm show < 3 ppm sensitivity and H₂O features remain essentially unchanged (< 2 ppm). The overall difference of 1.8 ppm confirms that the inclusion of sulfur chemistry does not alter the key molecular abundances or introduce systematic biases in our primary diagnostic species (CH₄, CO₂, H₂O, NH₃). We therefore adopt the simpler NCHO chemical network for the remainder of this work.

M-dwarf stars are particularly effective drivers of atmospheric photochemistry due to their enhanced UV emission relative to their bolometric luminosity, making the stars critical for understanding molecular dissociation and disequilibrium chemistry in sub-Neptune atmospheres (R. Hu et al. 2012; K. France et al. 2013). K2-18, classified as an M3-dwarf star with an effective temperature of 3457 ± 39 K (Table 1), provides an ideal case study for these photochemical processes (B. Benneke et al. 2019). Since UV measurements of K2-18 are not available, we adopted the GJ-176 stellar flux from K. France et al. (2013), modified by N. F. Wogan et al. (2024) as a proxy for K2-18 stellar flux. However, K2-18 appears to be more active than typical M dwarfs of its age, with multiple spot crossing events observed in Kepler data indicating significant stellar activity and variability (T. Barclay et al. 2021). While we assume the largely inactive GJ-176 UV spectrum for this analysis, the enhanced activity of K2-18 could potentially increase photochemical reaction rates and molecular dissociation beyond our current estimates. We used a standard two-stream Eddington coefficient of 0.5 to model the balance of upward and downward UV scattering in VULCAN. The model was configured with the planet’s known physical parameters (Table 1)

K2-18b’s equilibrium temperature of 254 ± 3.9 K (assuming albedo = 0.3; Table 1) indicates the potential for water condensation in the lower atmosphere. We enabled the condensation mode in VULCAN for H₂O only. We disabled gravitational settling of condensate particles to prevent excessive removal of water vapor from the upper atmosphere, which would unrealistically deplete stratospheric (H₂O). This approach is consistent with recent atmospheric modeling practices for K2-18b (N. F. Wogan et al. 2024) and similar sub-Neptune exoplanets (S.-M. Tsai et al. 2024), where careful treatment of condensation and transport processes is essential for accurate photochemical modeling

2.4. Generating Transmission Spectrum

Transmission spectra were computed using PICASO v3.0 by inputting the atmospheric composition profiles generated by VULCAN. For each atmospheric model, we extracted the pressure-temperature profile and molecular mixing ratios from VULCAN output and fed them into PICASO’s radiative transfer calculations. We configured PICASO with K2-18b’s measured planetary parameters and stellar properties from Table 1. Opacity calculations used a comprehensive molecular line database spanning 0.6–5.3 μm wavelengths at $R = 10,000$ spectral resolution (M. S. Marley et al. 2021). While the $R = 60,000$ database includes additional molecular species, we verified that using the higher-resolution database produced no significant spectral differences across our wavelength range for the atmospheric conditions and molecular abundances in our models. The $R = 10,000$ database includes the primary opacity contributors for our analysis: CH₄, CO, CO₂, H₂O, NH₃, H₂S, and alkali metals. The transmission spectrum calculation employed PICASO’s 1-D radiative transfer assuming a clear-sky atmosphere. Final spectra were binned to $R = 100$ resolution to match the JWST-NIRSpec/PRISM observations and facilitate comparison with published K2-18b spectra. Computing the transmission spectrum with coupled VULCAN-PICASO approach ensures self-consistent atmospheric composition and radiative transfer, providing realistic transmission spectra that account for both equilibrium and disequilibrium chemistry across our full parameter grid.

2.5. Benchmark Model

As we combined the radiative-convective and equilibrium chemistry code **PICASO** v3.0 with the disequilibrium chemistry and photochemistry code **VULCAN** to create model grids for K2-18b analogs, our approach differs from [N. F. Wogan et al. \(2024\)](#), who employed **PICASO** coupled with the **PHOTOCHEM** code ([N. F. Wogan et al. 2025](#)). To validate our modeling framework, we benchmark our results against the gas-rich sub-Neptune model from [N. F. Wogan et al. \(2024\)](#). While [N. F. Wogan et al. \(2025\)](#) demonstrated that **PHOTOCHEM** and **VULCAN** are highly consistent and produce nearly identical atmospheric compositions for the same inputs, our use of **VULCAN** provides another comprehensive photochemical and transport-driven disequilibrium network. The differences between packages arise mainly from their independent chemical kinetics databases, making both approaches complementary. Our **PICASO**-**VULCAN** framework enabled us to conduct a robust exploration of how interior heating and mixing processes shape observable spectral signatures in K2-18b and its analogs.

Using identical P-T profiles, variable variable (K_{zz}) profiles, stellar profiles, atmospheric metallicity, C/O ratio, elemental abundances, planetary mass and radius, orbital parameters, and boundary conditions from [N. F. Wogan et al. \(2024\)](#), our **VULCAN** simulation of K2-18b shows our predicted composition (Figure A1) matches across 0.5–5 μm . The most notable difference occurs around 2.5–3.0 μm , where our models exhibit 15.7 ppm enhanced absorption. The rest of the spectrum shows excellent agreement of less than 9 ppm differences. The difference appears to be how condensation is handled between the two codes. We attempted more aggressive condensation treatment to force that wavelength range to match the [N. F. Wogan et al. \(2024\)](#) spectrum, but this led to significantly depleted CO and CO₂ abundances, likely due to the removal of oxygen through enhanced water condensation. Outside of this wavelength range, we are in agreement with the [N. F. Wogan et al. \(2024\)](#) results. Other minor discrepancies may also be due to variations in reaction rate coefficients, molecular opacity databases, condensation treatments, or the specific implementation of vertical mixing and photochemical coupling between the two codes. The small magnitude of these differences and the good agreement between the two modeling systems confirms that our **PICASO**-**VULCAN** combined approach can be trusted and that our systematic exploration of intrinsic temperature and vertical mixing parameter space provides robust conclusions about atmospheric composition trends, with chemical network and condensation treatment uncertainties secondary to the dominant effects of thermal and dynamical parameters we investigate.

3. RESULTS

We present molecular abundances from our grid of atmospheric models for K2-18b spanning intrinsic temperatures (T_{int}) from 60 to 450 K and eddy diffusion coefficients (K_{zz}) from 10^5 - 10^{12} cm^2/s , along with the variable K_{zz} profile from [R. Hu \(2021\)](#); [N. F. Wogan et al. \(2024\)](#) in Figure 2. The parameter space encompasses a full range of plausible thermal and mixing states for temperate sub-Neptune atmospheres. Our analysis focuses on three complementary aspects of atmospheric structure and composition: mean molecular abundances in the photospheric region of pressures 10^{-3} - 10^{-4} bars (Section 3.1) probed by transmission spectroscopy, vertical abundance profiles revealing quenching and photochemical processes (Section 3.2), and transmission spectra showing observable signatures across 1–5 μm (Section 3.3). All abundance values discussed below are reported as \log_{10} volume mixing ratio unless otherwise noted.

3.1. Effect of Intrinsic Temperature and Vertical Mixing on Molecular Abundances

Figure 3 displays mean abundances of six key molecules: CH₄, CO, CO₂, NH₃, HCN, and H₂O averaged between pressures 10^{-3} and 10^{-4} bar. These pressure levels correspond to the photospheric region probed by transmission spectroscopy ([N. Madhusudhan et al. 2023](#)). The abundances at these altitudes reflect the complex interplay between deep atmospheric chemistry, vertical transport (quenching), and upper atmospheric photochemistry ([C. Visscher et al. 2010](#); [R. Hu 2021](#); [S.-M. Tsai et al. 2021](#)).

Our systematic exploration reveals distinct molecular behavior across three thermal regimes: (1) Cool temperature models ($T_{\text{int}} \leq 150$ K), (2) Intermediate temperature models (150 – 350 K), and (3) High temperature models ($T_{\text{int}} \geq 350$ K). These regimes exhibit fundamentally different chemical characteristics: temperature dominated species insensitive to mixing (CH₄, NH₃), moderately sensitive species showing coupled thermal dynamical effects (CO, H₂O, CO₂), and extreme disequilibrium tracers whose abundances vary by orders of magnitude with mixing strength (HCN). We organize our discussion using these temperature regime classifications throughout this section unless specific temperature values are noted.

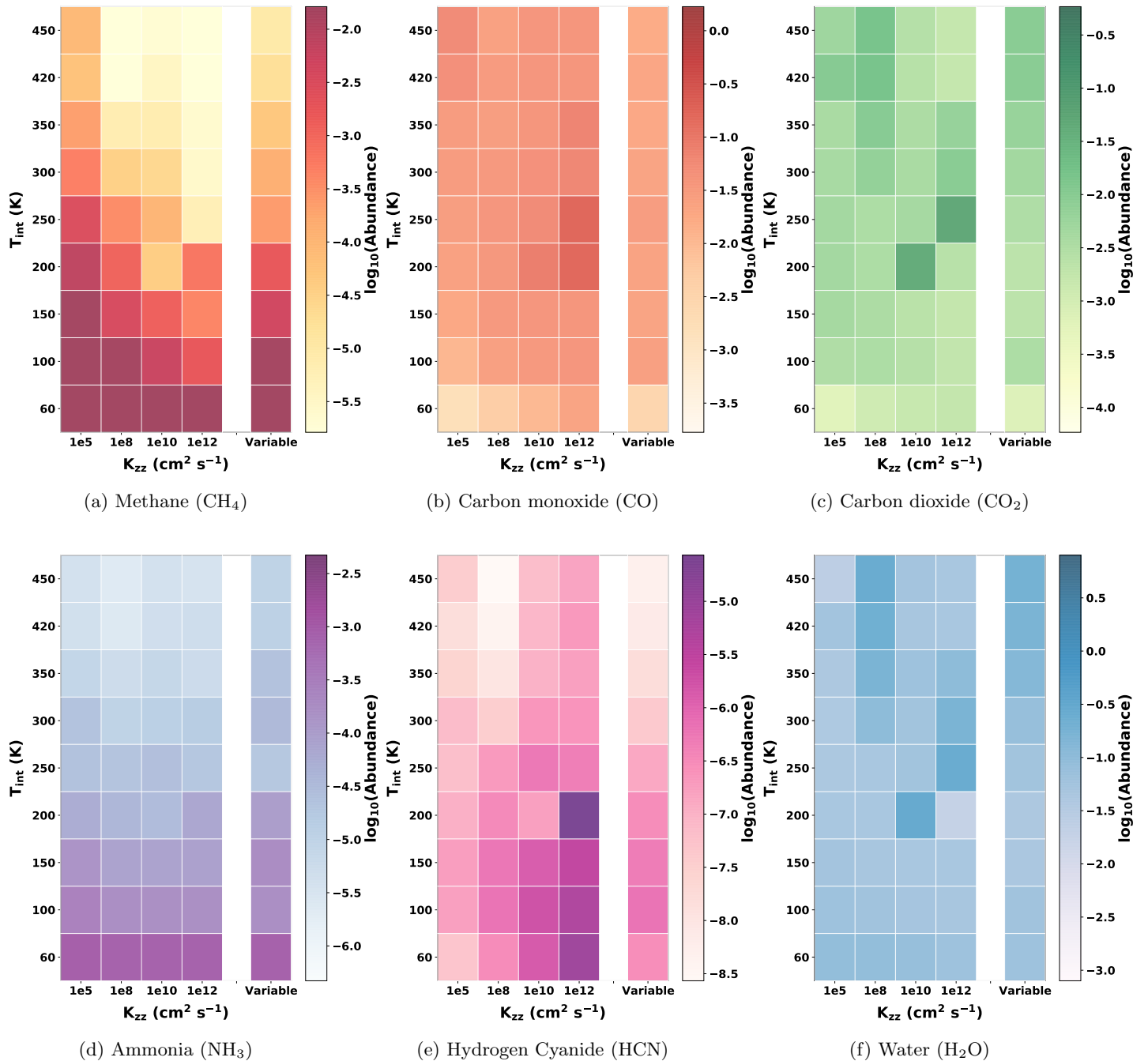


Figure 3. Mean \log_{10} abundance averaged over $10^{-3} - 10^{-4}$ bar as a function of intrinsic temperature (60 – 450 K, y-axis) and vertical eddy diffusion coefficient K_{zz} ($10^5 - 10^{12} \text{ cm}^2 \text{ s}^{-1}$, x-axis) for key atmospheric molecules: (a) methane (CH_4): yellow to orange, (b) carbon monoxide (CO): red dark to red, (c) carbon dioxide (CO_2): light green to dark green, (d) ammonia (NH_3): light blue to purple), (e) hydrogen cyanide (HCN): pink to magenta), and (f) water (H_2O): light blue to dark blue. More saturated colors (Darker) indicate higher abundances, while lighter colors indicate depletion. The column labeled **Variable** represents modeled grid using K_{zz} profile shown in Figure 2 as adopted from R. Hu (2021) and N. F. Wogan et al. (2024).

When comparing the variable K_{zz} profile from N. F. Wogan et al. (2024) (Figure 2) to constant K_{zz} profiles, different molecular species exhibit distinct sensitivity patterns that reveal the underlying atmospheric chemistry controls. CH_4 and NH_3 exhibit no difference between variable and constant K_{zz} cases, confirming thermochemical equilibrium dominance over vertical transport effects for these temperature-sensitive species. CO and H_2O (Figures 3b and 3f) show differences, with the variable profile tracking intermediate constant K_{zz} cases ($10^8 - 10^{10} \text{ cm}^2/\text{s}$) and differing by

< 0.5 dex across most temperatures. CO_2 (Figure 3c) shows enhanced abundances of 10^{-2} to $10^{-2.5}$ in intermediate temperature regimes with the variable 0.5–1.0 dex increase over most constant K_{zz} cases. Most notably, HCN (Figure 3e) exhibits the most dramatic behavioral change, shifting from primary K_{zz} sensitivity, with up to six orders of magnitude variation, in constant profiles to strongly temperature-dependent behavior with the variable K_{zz} profile. This indicates that altitude-dependent mixing creates asymmetric disequilibrium effects across thermal regimes (C. Visscher et al. 2010; S.-M. Tsai et al. 2021).

3.1.1. CH_4 , CO , CO_2

In cool intrinsic-temperature regimes, thermochemical equilibrium strongly favors CH_4 production through



such that CH_4 reaches abundances of 10^{-2} to 10^{-3} and exhibits strong temperature dependence but weak K_{zz} sensitivity, indicating thermochemical-equilibrium control (C. Visscher et al. 2006; J. I. Moses et al. 2011). As temperature increases to intermediate regimes (200–350 K), CH_4 abundances decrease to 10^{-3} to 10^{-4} , while at high temperatures (> 350 K) severe depletion occurs, with abundances dropping to 10^{-5} to 10^{-6} as the equilibrium reverses to favor CO production.

CO exhibits weaker temperature sensitivity, with abundances ranging from $10^{-0.5}$ to 10^{-1} across most of parameter space, and shows systematic enhancement at higher intrinsic temperatures as it becomes the thermodynamically favored carbon carrier (C. Visscher et al. 2006). Unlike CH_4 , CO is photochemically stable due to its strong $\text{C}\equiv\text{O}$ triple bond, making it largely immune to stellar-UV destruction.

CO_2 demonstrates the most complex behavior, reaching peak abundances of 10^{-2} to $10^{-2.5}$ in intermediate-temperature models where it serves as a diagnostic for moderately heated interior conditions. CO_2 becomes depleted in both cool and hot regimes, but shows strong K_{zz} dependence under intermediate conditions.

The dominance of interior thermal processes over photochemistry becomes clear when examining carbon speciation. While upper-atmosphere photochemical pathways produce negligible CO and CO_2 , deep hot interiors dramatically enhance these species through efficient vertical transport of thermochemically equilibrated gas from depth (J. I. Moses et al. 2011; C. Visscher & J. I. Moses 2011). This deep quenching process simultaneously suppresses CH_4 before it reaches the photochemical zone, creating a fundamental asymmetry: CH_4 can be destroyed by both thermal equilibrium and photochemistry, whereas CO and CO_2 are produced thermally and remain photochemically stable.

3.1.2. NH_3

NH_3 behavior reflects the complex interplay between thermochemical equilibrium and photochemical processes in nitrogen chemistry (K. Heng & S.-M. Tsai 2016). In cool temperature regimes, thermochemical equilibrium favors NH_3 production through



producing high abundances of $10^{-2.5}$ to 10^{-3} (Figure 3d). However, NH_3 chemistry is fundamentally more complex than carbon chemistry due to the chemical inertness of N_2 . NH_3 is thermochemically favored under cool temperatures and high pressures, but the equilibrium with N_2 ($2 \text{NH}_3 \rightleftharpoons \text{N}_2 + 3 \text{H}_2$) becomes increasingly unfavorable as temperature rises, since N_2 is chemically inert and the reaction kinetics are sluggish.

This thermal sensitivity is compounded by photochemical fragility. Unlike the carbon-bearing species CO and CO_2 , which are photochemically stable, NH_3 is readily destroyed by stellar UV radiation (X. Yu et al. 2021; R. Hu 2021; S.-M. Tsai et al. 2021). The degree of photochemical depletion depends critically on stellar type, as M dwarf stars provide the near-UV irradiation needed for NH_3 photodissociation (X. Yu et al. 2021).

However, our models using the K2-18 stellar flux from N. F. Wogan et al. (2024) show NH_3 abundances remaining relatively constant across our grid, with high intrinsic temperature thermal depletion to $10^{-5.5}$ being the dominant effect rather than photochemical destruction, despite the known stellar activity of this M dwarf (T. Barclay et al. 2021). This thermal control over NH_3 abundances, combined with its weak K_{zz} sensitivity, indicates that interior temperature rather than atmospheric mixing or photochemistry primarily determines observable nitrogen speciation in our K2-18b analog models.

3.1.3. H_2O

H_2O exhibits minimal sensitivity to both intrinsic temperature and vertical mixing strength (Figure 3f). H_2O maintains stable abundances across the entire parameter space, ranging from approximately $10^{-0.5}$ to $10^{-1.5}$, showing little systematic variation (Appendix Table A1). This behavior reflects two key factors: (1) H_2O 's thermodynamic stability in hydrogen-dominated atmospheres, where it remains the dominant oxygen-bearing species across a wide range of conditions (C. Visscher et al. 2006), and (2) the fact that our atmospheric temperature profiles remain above the H_2O condensation curve throughout most of the observable atmosphere. Water condensation occurs at approximately 270 K at 1 bar, but our pressure–temperature profiles show temperatures exceeding this threshold at 1 bar for most intrinsic-temperature models, preventing significant condensation depletion in the photospheric region (10^{-3} – 10^{-4} bar) probed by transmission spectroscopy.

The uniform abundance distribution across our intrinsic temperature range (60–450 K) and vertical mixing strength range (10^5 – 10^{12} cm²/s) indicates that H_2O abundances are controlled primarily by the bulk atmospheric metallicity and C/O ratio rather than by local chemical equilibrium or transport processes. Additionally, part of this muted response reflects the fundamental control of the C/O ratio on water abundance. With our assumed solar C/O ratio (0.5), excess oxygen beyond that consumed by CO formation is available to form H_2O , maintaining relatively stable abundances across thermal conditions. In high C/O ratio atmospheres (C/O > 1), carbon would consume nearly all available oxygen to form CO, leaving water virtually absent regardless of metallicity or temperature (N. Madhusudhan 2012; J. I. Moses et al. 2011). This makes H_2O a valuable diagnostic of atmospheric C/O ratio, with its abundance primarily determined by the initial elemental composition rather than local thermochemical processes (K. I. Öberg et al. 2011; N. Madhusudhan 2012).

Even at the highest intrinsic temperatures, where other molecules like CH_4 and NH_3 show dramatic depletion, H_2O remains comparatively unaffected due to its high thermodynamic stability and its role as a primary oxygen reservoir under these conditions. This insensitivity to both thermal and mixing parameters makes H_2O a poor diagnostic for constraining interior thermal structure or atmospheric dynamics, but an excellent tracer of bulk atmospheric composition and metallicity in sub-Neptune atmospheres.

3.1.4. HCN

Hydrogen cyanide (HCN) exhibits the most complex atmospheric behavior, with extreme sensitivity to both T_{int} and K_{zz} (Figure 3e). Our analysis reveals that photochemistry strongly couples NH_3 and HCN abundances, with HCN becoming the primary photochemical product of NH_3 in CH_4 -rich environments (J. I. Moses et al. 2011; R. Hu 2021; S.-M. Tsai et al. 2023).

HCN abundances displays variability across our parameter grid. At high temperatures with low 10^5 cm²/s, HCN reaches peak abundances of approximately 10^{-5} to 10^{-7} . However, the K_{zz} sensitivity is extreme: abundances vary by up to 6 orders of magnitude as K_{zz} increases from 10^5 – 10^{12} cm²/s. For $K_{zz} \gtrsim 10^{10}$ cm²/s, HCN abundances plummet to the lowest values in our grid, while at low temperatures, HCN becomes depleted regardless of mixing strength (Appendix Table A1).

This extraordinary sensitivity reflects competing formation and destruction processes operating across different atmospheric regions. HCN forms through coupled NH_3 + CH_4 photochemistry in the upper atmosphere (10^{-4} – 10^{-2} bar), where stellar UV drives the reaction sequence:



The availability of atomic nitrogen from NH_3 photodissociation proves critical for HCN formation, making this species directly dependent on both parent molecules (K. Zahnle et al. 2009; J. I. Moses et al. 2011; S.-M. Tsai et al. 2021).

However, intrinsic temperature exerts indirect control by governing the initial supply of NH_3 and CH_4 from the deep atmosphere. Additionally, while HCN can form efficiently in hot interior layers, it faces rapid destruction in cooler upper regions through UV photolysis and oxidation by O and OH radicals (P. B. Rimmer et al. 2020). This

creates a fundamental competition: weak mixing (low K_{zz}) preserves HCN formed at depth, while strong mixing rapidly transports HCN to destruction-dominated regions (K. Zahnle et al. 2009; J. I. Moses et al. 2011; R. Hu 2021). The extreme K_{zz} sensitivity therefore reflects this balance between transport-controlled quenching in the deep interior and photochemical processing in the observable atmosphere, making HCN a diagnostic of both thermal structure and atmospheric dynamics.

However, intrinsic temperature exerts indirect control by governing the initial supply of NH_3 and CH_4 from the deep atmosphere that serve as HCN precursors. HCN formation occurs primarily in the upper atmosphere (10^{-4} to 10^{-2} bar) through photochemical pathways requiring UV-dissociated NH_3 and CH_4 , rather than through thermal processes in the deep interior where thermochemical equilibrium favors N_2 and CH_4 . Once formed photochemically, HCN faces rapid destruction in the upper atmosphere through continued UV photolysis and oxidation by O and OH radicals (P. B. Rimmer et al. 2020). This creates a fundamental competition: weak mixing (low K_{zz}) allows HCN to accumulate in its formation region, while strong mixing rapidly transports HCN to destruction-dominated regions or dilutes it with HCN-poor gas from below (K. Zahnle et al. 2009; J. I. Moses et al. 2011; R. Hu 2021). The extreme K_{zz} sensitivity therefore reflects this balance between photochemical production and destruction in the observable atmosphere, making HCN a diagnostic of both photochemical activity and atmospheric dynamics.

3.2. Vertical Abundance Profiles and Atmospheric Structure

Quenching occurs when vertical mixing timescales become comparable to chemical equilibration timescales, causing molecular abundances to freeze out and deviate from local thermochemical equilibrium (C. Visscher et al. 2010; J. I. Moses et al. 2011). The quench pressure, the atmospheric level where this transition from equilibrium to transport control occurs, varies systematically with K_{zz} , T_{int} , and molecular species (C. Visscher et al. 2010; J. I. Moses et al. 2011).

Figure 4 reveals three distinct atmospheric regimes governing molecular distributions. In the deep equilibrium region ($\gtrsim 100$ bar), all molecules rapidly adjust to thermochemical equilibrium (C. Visscher et al. 2006). Quenching manifests as a characteristic “kink” in abundance profiles where chemical timescales exceed mixing timescales, followed by flat vertical profiles where quenched abundances are transported upward and remain constant until molecular diffusion dominates (C. Visscher et al. 2010).

The depth of quenching varies dramatically with mixing strength. For weak mixing ($10^5 \text{ cm}^2/\text{s}$), quenching occurs between 10^{-1} to 10^1 bar for most species. As mixing strengthens to $10^8 \text{ cm}^2/\text{s}$, quench points deepen to 10^{-1} – 1 bar, and under extremely strong mixing (10^{10} – $10^{12} \text{ cm}^2/\text{s}$), quenching shifts to 1 – 10 bar. This systematic deepening enables high-temperature chemistry from deep layers to reach the observable photosphere (10^{-3} – 10^{-4} bar).

Different molecules exhibit distinct sensitivities to this quenching behavior, reflecting fundamentally different chemical processes. CH_4 and NH_3 show minimal quench-pressure variation across K_{zz} values, reflecting rapid equilibration timescales that keep pace with even vigorous vertical mixing (C. Visscher et al. 2010). For these thermochemically controlled species, the quench point preserves deep interior abundances by “freezing” them when transport becomes faster than chemistry.

HCN demonstrates extreme sensitivity, but through an opposite mechanism. Unlike CH_4 and NH_3 , HCN is not formed in thermochemical equilibrium in the deep interior. Instead, it is photochemically produced in the upper atmosphere and then transported downward by mixing. The “quench point” for HCN represents the level where it is thermochemically destroyed and converted back to NH_3 , CH_4 , and other equilibrium species, rather than preserved (J. I. Moses et al. 2011; K. Zahnle et al. 2009). At high temperatures with weak mixing ($K_{zz} = 10^5 \text{ cm}^2/\text{s}$), this destruction occurs at shallow depths (~ 0.1 bar), allowing HCN to accumulate in the observable atmosphere. Under strong mixing ($K_{zz} = 10^{12} \text{ cm}^2/\text{s}$), vigorous transport carries HCN deeper into the hot interior where destruction is efficient, causing severe depletion despite continuous photochemical production above.

The variable- K_{zz} profile from N. F. Wogan et al. (2024) produces intermediate quenching behavior for equilibrium-dominated species (CH_4 , NH_3 , CO , H_2O). However, HCN experiences asymmetric effects: enhanced mixing at low pressures drives deeper quenching than expected, particularly affecting cool intrinsic models where the photosphere samples these strongly mixed upper layers. This altitude dependent mixing causes HCN to exhibit high K_{zz} like depletion in cool regimes despite weaker deep mixing (J. I. Moses et al. 2011; S.-M. Tsai et al. 2021).

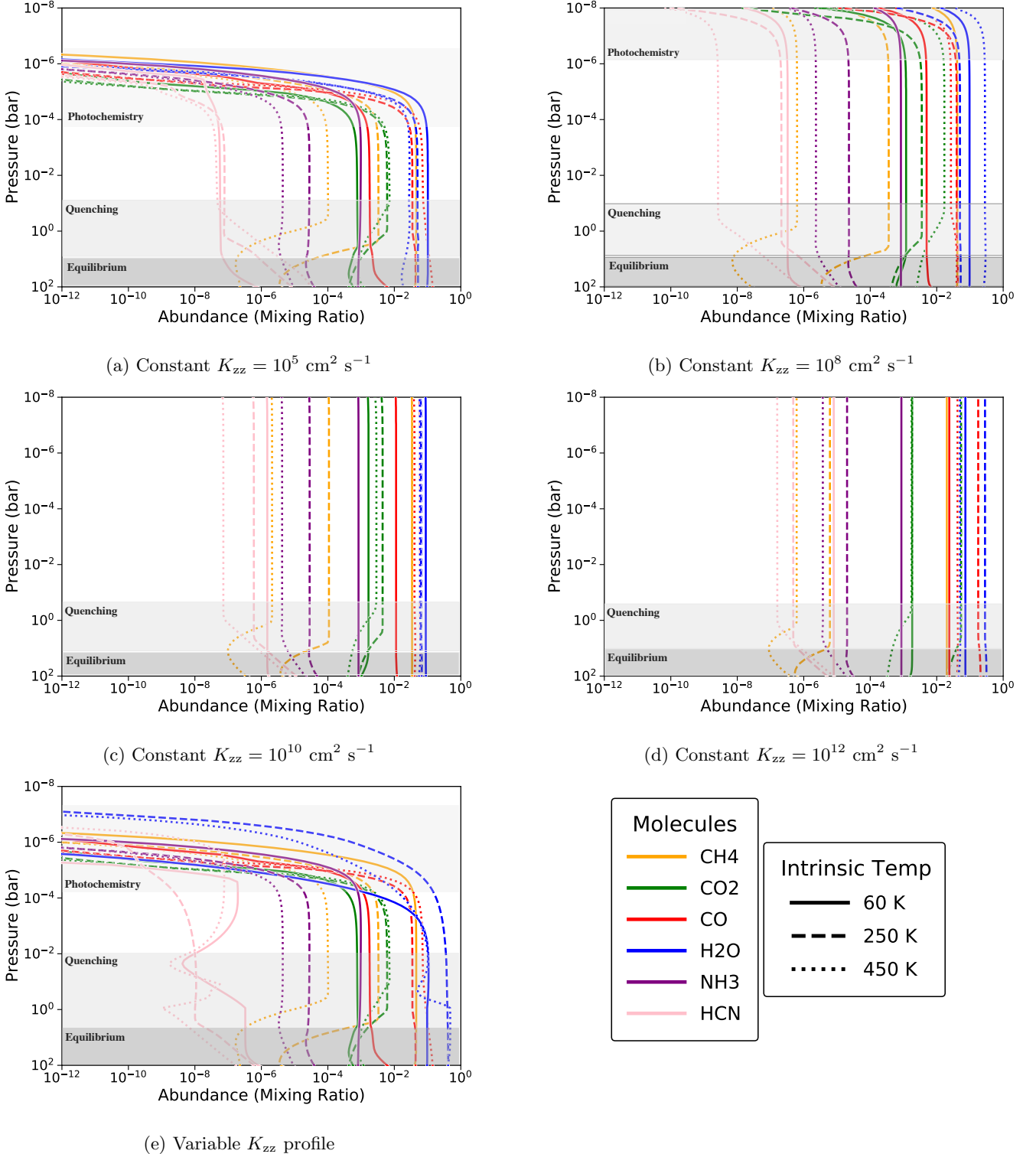


Figure 4. Vertical abundance profiles of key atmospheric molecules as a function of pressure for mini-Neptune models with different eddy diffusion prescriptions. Panels (a)–(d) show constant K_{zz} cases: 10^5 , 10^8 , 10^{10} , and $10^{12} \text{ cm}^2 \text{ s}^{-1}$. Panel (e) shows the variable- K_{zz} case adopted from R. Hu (2021) and N. F. Wogan et al. (2024). Each panel shows mixing-ratio profiles for CH₄ (blue), CO₂ (green), CO (orange), H₂O (red), NH₃ (purple), and HCN (pink) at three intrinsic temperatures: 60 K (solid lines), 250 K (dashed lines), and 450 K (dotted lines). The atmosphere is divided into three regions: the equilibrium zone (dark gray, > 100 bar), the quenching zone (gray, 1–100 bar), and the photochemistry zone (light gray, < 1 bar).

At pressures below 10^{-4} bar, abundance profiles deviate from quenched values as UV photolysis becomes dominant. This photochemical region is most prominent under weak mixing ($K_{zz} = 10^5 \text{ cm}^2/\text{s}$) and variable- K_{zz} conditions, where molecules like CH_4 , H_2O , and NH_3 undergo photodissociation, creating radicals (CH_3 , OH , NH_2) that drive secondary chemistry (J. I. Moses et al. 2011; R. Hu 2021). Our treatment considers gas-phase photochemistry only and excludes photochemical haze formation and associated radiative effects. The photochemical layer thickness decreases with increasing K_{zz} as strong vertical transport creates a two-way exchange: upward transport continuously replenishes photolyzed parent molecules from below, while downward transport carries photochemical products into deeper layers where they are thermochemically converted back to their parent species. For $K_{zz} > 10^{10} \text{ cm}^2/\text{s}$, photochemical effects become negligible as mixing timescales far exceed destruction timescales, effectively creating a well-mixed atmosphere where photochemical signatures are diluted.

These vertical profiles demonstrate that observable atmospheric composition (10^{-3} – 10^{-4} bar) results from the combined influence of deep quenched abundances, condensation processes, and upper atmosphere photochemistry rather than local thermochemical equilibrium. The systematic K_{zz} and temperature dependence of quench pressures provides a diagnostic framework for constraining thermal structure (T_{int}), mixing efficiency (K_{zz}), and condensation efficiency through molecular abundance ratios, enabling us to break parameter degeneracies in atmospheric interpretation (S.-M. Tsai et al. 2021; N. Madhusudhan et al. 2023; N. F. Wogan et al. 2024).

3.3. Transmission Spectra

Figures 5 and 6 present transmission spectra across our model grid from 0.5–5 μm , demonstrating how intrinsic temperature and vertical mixing control observable spectral signatures. The molecular abundance patterns discussed in Section 3.1 translate directly into characteristic spectral features that distinguish thermal regimes and mixing conditions.

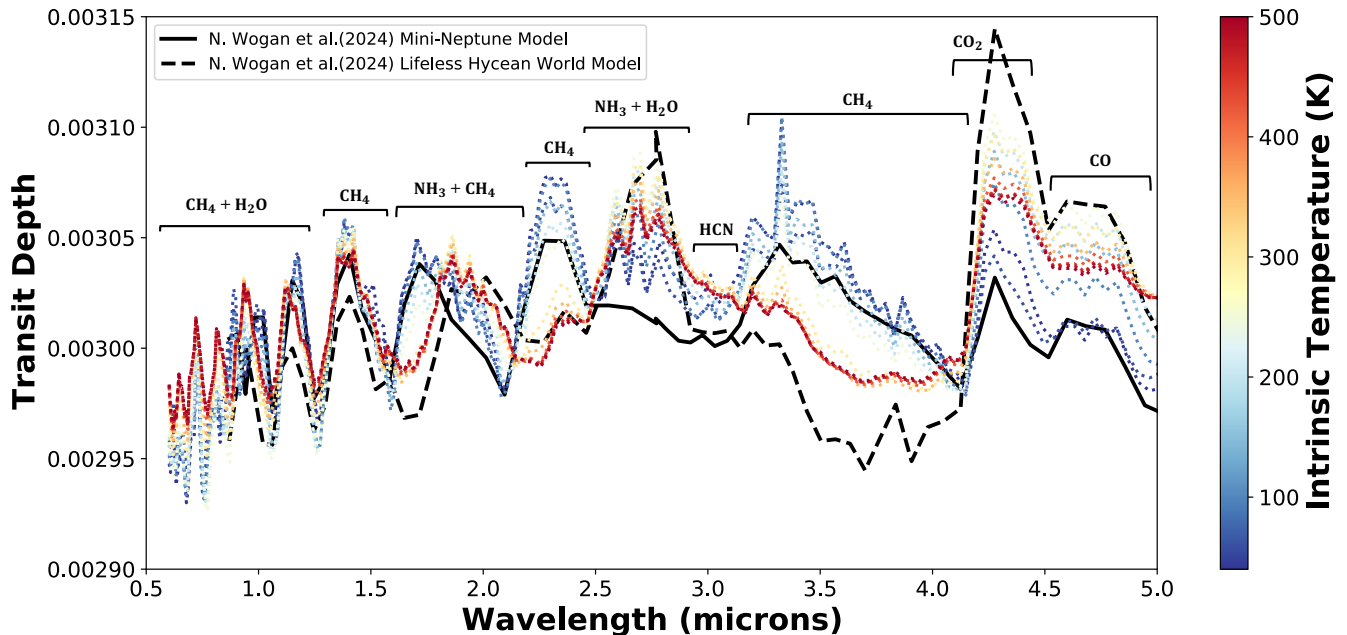


Figure 5. Spectrum grid with varying intrinsic temperature and K_{zz} profile. The K_{zz} profile follows the parameterization from N. F. Wogan et al. (2024) for mini-Neptune atmospheres. The grid showcases atmospheric temperature pressure profiles spanning intrinsic temperatures (T_{int}) from 60 to 450 K with the K_{zz} profile applied across all models, while metallicity and C/O ratio are held constant. Note that the benchmark spectrum (black line) exhibits some artificially sharp features due to the spectral resolution and binning used in the original N. F. Wogan et al. (2024) analysis, which we maintain for direct comparison.

Figure 5 shows systematic spectral evolution with intrinsic temperature using the variable- K_{zz} profile. Cool T_{int} models ($T_{\text{int}} \leq 150$ K) exhibit strong CH_4 features at 1.4, 2.3, and 3.3 μm , accompanied by prominent $\text{NH}_3 + \text{CH}_4$

absorption at 1.5 and 2.0 μm (J. J. Fortney 2005; N. Madhusudhan et al. 2023). These signatures reflect the high CH_4 and NH_3 abundances produced by favorable thermochemical equilibrium at low temperatures (C. Visscher et al. 2006; J. I. Moses et al. 2011). Intermediate models ($T_{\text{int}} = 200\text{--}350\text{ K}$) show progressive weakening of CH_4 features with concurrent strengthening of CO_2 absorption at 4.3 μm , capturing the transition from reducing to more oxidized atmospheric chemistry. Hot T_{int} models ($T_{\text{int}} \geq 350\text{ K}$) display severely depleted CH_4 features across all diagnostic wavelengths, with dominant H_2O absorption and emerging CO features at 4.6 μm reflecting the thermochemical dominance of oxidized carbon species (J. I. Moses et al. 2011; S.-M. Tsai et al. 2021).

Crucially, our intermediate models ($T_{\text{int}} = 300\text{--}350\text{ K}$) show systematic convergence toward the N. F. Wogan et al. (2024) sub-Neptune benchmark, reaching a difference of 34 ppm across 0.9–5.1 μm . The agreement varies by molecular region: excellent convergence occurs for the primary CH_4 diagnostic band at 3.3 μm (10 ppm), while larger systematic offsets appear in 2.5–3.0 μm ; (53 ppm) and CO_2/CO bands (4.3–4.6 μm ; 44–66 ppm). Despite these localized discrepancies, the overall spectral morphology and dominant molecular absorption signatures remain consistent, indicating that this thermal regime reproduces the characteristic sub-Neptune spectrum while capturing subtle differences in atmospheric chemistry parameterization. This convergence occurs precisely where our abundance analysis indicates favorable CO_2/CH_4 ratios and balanced thermochemistry and transport interactions.

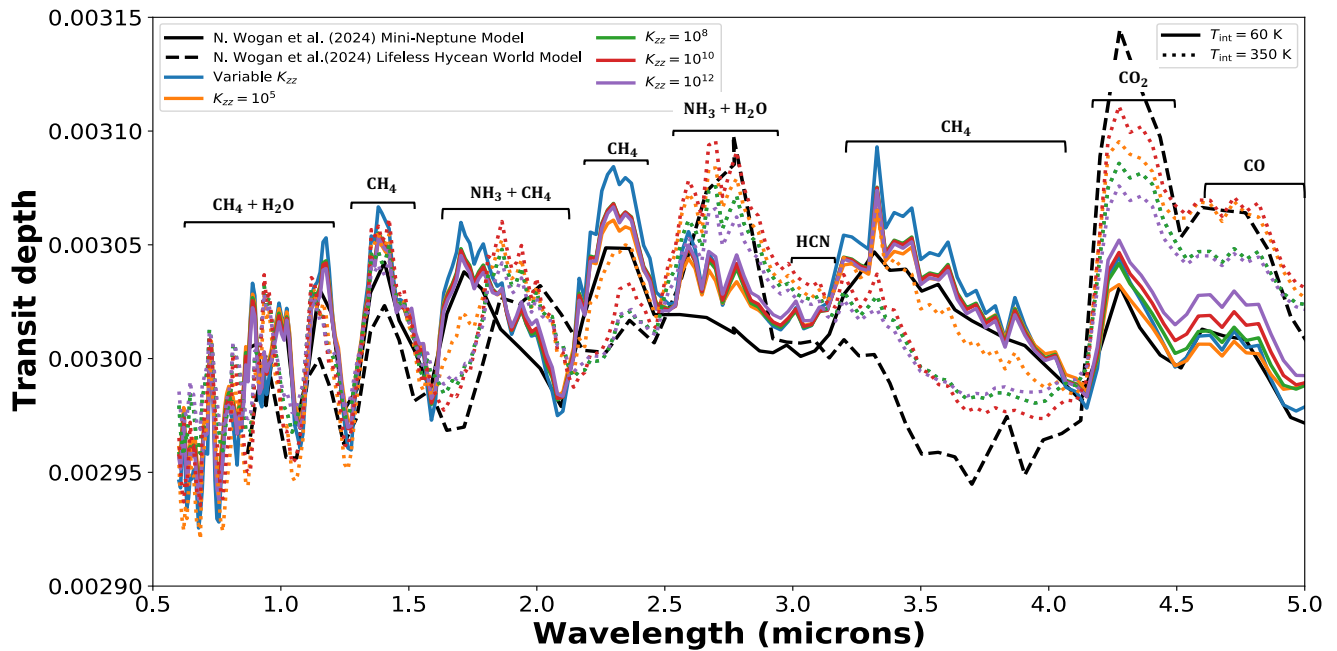


Figure 6. Transmission spectra for K2-18b analog atmospheres with fixed intrinsic temperature ($T_{\text{int}} = 60\text{ K}$) and varying vertical eddy diffusion coefficients (K_{zz}). The spectra span six orders of magnitude in mixing strength from $K_{\text{zz}} = 10^5$ to $10^{12}\text{ cm}^2\text{ s}^{-1}$ (colored lines), along with the variable K_{zz} profile from N. F. Wogan et al. (2024) (blue line). The N. F. Wogan et al. (2024) mini-Neptune benchmark model is shown in black for comparison.

Figure 6 reveals the contrasting role of vertical mixing at fixed cool temperature ($T_{\text{int}} = 60\text{ K}$). Despite spanning six orders of magnitude in K_{zz} (10^5 to $10^{12}\text{ cm}^2\text{ s}^{-1}$), the transmission spectra show similarity in their primary molecular features. The CH_4 absorption bands at 1.4, 2.3, and 3.3 μm remain virtually unchanged across all mixing strengths, as do the NH_3 features at 1.5 and 2.0 μm (J. J. Fortney 2005; N. Madhusudhan et al. 2023). This spectral insensitivity confirms that at cool temperatures, thermochemical equilibrium dominates over transport effects, with molecular abundances controlled by local temperature rather than vertical mixing efficiency (C. Visscher et al. 2006, 2010; J. I. Moses et al. 2011).

However, subtle differences do emerge in specific wavelength regions. The CO_2 feature at 4.3 μm shows modest variation with K_{zz} , reflecting the moderate mixing sensitivity identified in our abundance analysis. Additionally, the variable- K_{zz} profile from N. F. Wogan et al. (2024) produces spectra that fall within the range of constant-mixing

models, validating our systematic exploration approach. The convergence of all cool-temperature spectra toward similar morphologies, regardless of mixing strength, highlights that thermal state, not atmospheric dynamics, provides the primary spectral diagnostic for mini-Neptune characterization.

These systematic spectral trends and benchmark convergence provide observational constraints on atmospheric thermal state and mixing efficiency, establishing a framework for distinguishing between competing atmospheric scenarios through transmission spectroscopy, with detailed diagnostic implications discussed in Section 4.

4. DISCUSSION

Our systematic exploration of intrinsic temperature and vertical mixing parameter space reveals fundamental insights that extend and complement previous sub-Neptune atmospheric studies. While earlier investigations focused primarily on surface depth effects (e.g., X. Yu et al. 2021), atmospheric metallicity variations (e.g., A. Y. Jaziri et al. 2025), and stellar irradiation impacts (e.g., R. Hu et al. 2025), our work demonstrates that interior thermal state and vertical transport parameters typically held fixed, exert comparable control over observable atmospheric composition. The convergence of our intermediate-temperature models ($T_{\text{int}} = 300\text{--}350$ K) with the N. F. Wogan et al. (2024) K2-18b benchmark establishes that moderately heated sub-Neptunes can reproduce observed spectral signatures through deep thermochemical processes alone, creating substantial degeneracy with shallow-surface Hycean world scenarios. This finding challenges the conventional approach of inferring planetary composition from atmospheric spectra without systematic exploration of thermal and mixing parameter space. The distinct sensitivity regimes we identify, from temperature-dominated species (CH_4, NH_3) to extreme disequilibrium tracers (HCN), provide new diagnostic frameworks for distinguishing between competing atmospheric scenarios. These results have direct implications for interpreting current JWST observations, designing future observational strategies, and reassessing the census of potentially habitable worlds among the sub-Neptune population.

4.1. *Justification for Parameter Space*

Our systematic exploration reveals that intrinsic temperatures ranging from $T_{\text{int}} = 60\text{--}450$ K produce significant changes in the retrieved molecular abundances and observable transmission spectrum (Figure 3). We note that the extreme range in intrinsic temperatures is plausible for sub-Neptunes. Gravitational contraction represents a primary heat source, with cooling timescales extending to 1 Gyr for planets in the $2\text{--}8 M_{\oplus}$ mass range (J. J. Fortney et al. 2020). Radiogenic heating from long-lived isotopes (e.g., $^{26}\text{Al}, ^{40}\text{K}, \text{U}, \text{Th}$) can also provide sustained interior heat over geological timescales (H. Lammer et al. 2018), while the retention of substantial H/He envelopes impedes radiative heat loss and can maintain elevated intrinsic temperatures over extended periods (E. D. Lopez & J. J. Fortney 2014). Tidal heating from eccentric or obliquity tides can further dump heat into the interior of the planet throughout its lifetime, enabling even older planets to maintain heated interiors (S. Millholland 2019; S. Millholland et al. 2020). Recent observations of the more massive sub-Saturn, WASP-107b, determine a T_{int} of 460 ± 40 K, an artifact of ongoing tidal heating (D. K. Sing et al. 2024).

On the other hand, older planets not experiencing an ongoing source of heat are expected to cool over time. Atmospheric models (J. J. Fortney et al. 2011; T. Guillot 2010; D. Thorngren et al. 2019) often assume T_{int} between 40–100 K for planets older than several billion years. However, even in our own Solar System, it is unclear what scenarios control the T_{int} of our gas giants. Neptune outputs nearly 3× more internal heat than Uranus, despite their similarities in size and composition (T. Guillot & D. Gautier 2015). Therefore, without knowing the evolutionary history of sub-Neptunes, exploring the full range of plausible intrinsic temperatures is required for deriving atmospheric composition and structure.

While less of a driver of disequilibrium chemistry, K_{zz} impacts the quench pressure level and overall mixing of the observable pressures in an atmosphere. Observational constraints, however, are limited. Measured K_{zz} in our Solar System gas giants vary from 10^6 to $10^9 \text{ cm}^2 \text{ s}^{-1}$ (J. I. Moses et al. 2011; X. Zhang & A. P. Showman 2018), while theoretical models suggest a range of K_{zz} from 10^5 to $10^{12} \text{ cm}^2 \text{ s}^{-1}$ (V. Parmentier et al. 2013; X. Zhang & A. P. Showman 2018). Given the limited observational constraints on the vertical mixing of sub-Neptunes, we explored a wide range of constant K_{zz} profiles alongside the variable K_{zz} profile adopted from N. F. Wogan et al. (2024). Comparing our transmission spectra across these different mixing assumptions reveals remarkably similar observable signatures. The variable K_{zz} profile produces spectral features that closely match those from constant K_{zz} cases in

the 10^8 – 10^{10} cm 2 s $^{-1}$ range, with differences of less than 5 ppm in key diagnostic wavelengths (1.4, 2.3, and 3.3 μ m for CH $_4$; 4.3 μ m for CO $_2$). Even for molecules most sensitive to mixing strength, such as HCN, the variable profile behavior falls within the envelope of constant K_{zz} predictions rather than representing a fundamentally distinct regime.

This spectral similarity demonstrates that for atmospheric characterization purposes, assuming a constant K_{zz} profile provides a robust approximation to more complex, altitude-dependent mixing scenarios. The choice between constant and variable K_{zz} parameterizations introduces uncertainties smaller than current observational precision, validating the use of constant K_{zz} grids for interpreting sub-Neptune transmission spectra. This finding is particularly important for atmospheric retrievals, where computational efficiency often requires simplified mixing prescriptions.

4.2. In Context with Previous sub-Neptune Work

Our approach draws from multiple atmospheric modeling frameworks to understand compositional degeneracies in sub-Neptune atmospheres. In particular, our work builds on the framework developed by X. Yu et al. (2021), who showed that surface depth controls how molecules behave in sub-Neptune atmospheres. In their model, deep atmospheres without surfaces allow CH $_4$ and NH $_3$ to be recycled: these molecules are destroyed by starlight in the upper atmosphere, but vertical mixing carries them down to hot deep layers where they reform, and then transports them back upward. This recycling process prevents molecular abundances from being completely eroded by stellar radiation.

However, shallow surfaces at around 10 bar pressure cut off this recycling. In Hycean world scenarios, a water ocean surface stops the atmosphere early, so destroyed CH $_4$ and NH $_3$ molecules cannot reach the deep hot layers to be reformed (X. Yu et al. 2021). Instead, these molecules are continuously destroyed without replacement, leading to depleted abundances and more oxidized chemistry with CO and CO $_2$.

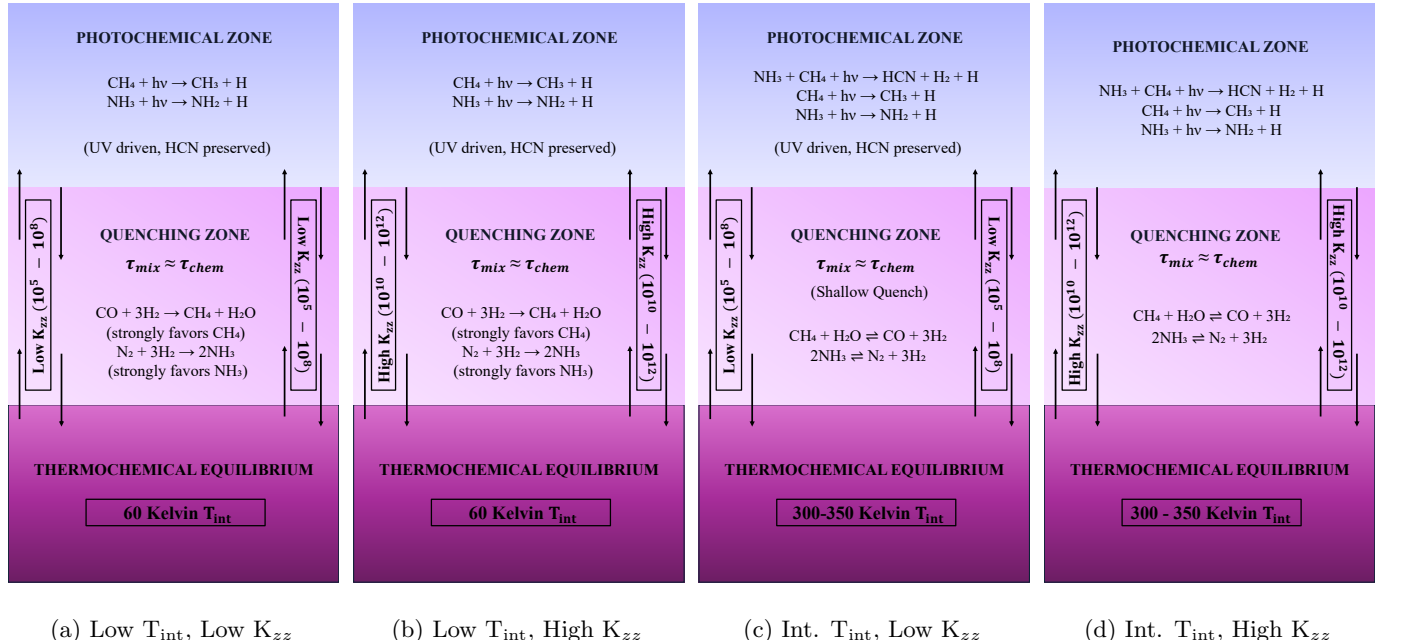


Figure 7. Schematic illustration of atmospheric chemistry regimes for different intrinsic temperature and vertical mixing combinations in K2-18b analogs. The atmosphere is divided into three regions: the equilibrium zone (purple, deep atmosphere), the quenching zone (pink, where $\tau_{\text{mix}} \approx \tau_{\text{chem}}$), and the photochemistry zone (blue, upper atmosphere). (a) Cool interior with weak vertical mixing (b) Cool interior with strong vertical mixing (c) Intermediate temperature with weak vertical mixing (d) Intermediate temperature with strong vertical mixing

Our quantitative analysis reveals that conditions for reproducing K2-18b's molecular signatures occur when chemical (τ_{chem}) and mixing timescales,

$$\tau_{\text{mix}} = \frac{L^2}{K_{zz}}, \quad (8)$$

converge under intermediate intrinsic temperatures ($T_{\text{int}} = 250\text{--}350\text{ K}$; $K_{zz} = 10^8\text{--}10^{10}\text{ cm}^2\text{s}^{-1}$). For CH₄, chemical timescales accelerate by a factor of ten from cool to hot conditions, while mixing timescales span four orders of magnitude across our K_{zz} range. This convergence deepens quench pressures from 10⁸ bar to 10⁷ bar, enabling transport of interior chemistry to observable altitudes, analogous to quenching behavior in Jupiter's atmosphere (J. I. Moses et al. 2011).

Figure 7 illustrates how these processes combine in K2-18b analogs. Cool interior models consistently produce CH₄-rich atmospheres regardless of mixing strength, failing to match observations. However, intermediate-temperature models with strong mixing achieve the moderate CH₄ depletion and CO₂ enhancement observed by JWST (N. Madhusudhan et al. 2023). Remarkably, this produces molecular patterns similar to Hycean predictions but through fundamentally different mechanisms: deep-interior processes in thick atmospheres rather than surface–ocean chemistry in thin ones. Our transmission spectra demonstrate this degeneracy directly. Models with intermediate intrinsic temperatures ($T_{\text{int}} = 300\text{--}350\text{ K}$) closely reproduce the N. F. Wogan et al. (2024) K2-18b benchmark spectrum with differences of only 14.5 ppm across 0.5–5 μm , despite representing entirely different planetary scenarios. The spectral convergence occurs because both pathways can produce similar CH₄ depletion and CO₂ enhancement: Hycean worlds achieve this through photochemical destruction at shallow surfaces with no recycling, while our heated sub-Neptunes reach the same observable outcome through thermochemical quenching in deep, hot interiors transported upward by vertical mixing. This atmospheric complexity where systematic variations in just two parameters (T_{int} and K_{zz}) can reproduce the spectral signatures previously attributed to fundamentally different planet types reveals that transmission spectroscopy alone may be insufficient to distinguish between competing atmospheric scenarios without additional diagnostics.

However, our parameter study reveals diagnostic opportunities through mixing sensitive molecular tracers. Species that form in deep atmospheric layers but face destruction in upper regions provide the clearest tests while some atmospheric scenarios might preserve these tracers, vigorous vertical transport can carry them to regions where chemical loss dominates (Example: HCN) (J. I. Moses et al. 2011; S.-M. Tsai et al. 2021). The specific conditions we identify ($T_{\text{int}} = 300\text{--}350\text{ K}$ with strong mixing) provide concrete observational targets for constraining planetary interiors and atmospheric dynamics (X. Zhang & A. P. Showman 2018). Our results demonstrate that interpreting sub-Neptune atmospheres requires considering both surface conditions and interior thermal evolution. Future work should systematically explore how these processes combine across the full range of sub-Neptune properties to better understand this abundant planetary class (B. J. Fulton et al. 2017; L. A. Rogers 2015).

4.3. Constraints of this Work

This work presents a comprehensive analysis of the intrinsic temperature and vertical mixing coefficient parameter space, we acknowledge that assumptions made do not capture the full range of possibilities for characterizing the complexities of sub-Neptune atmospheres. While observationally supported for K2-18b and other sub-Neptunes, we hold the atmospheric composition constant to a 100× solar metallicity and a solar C/O ratio, which constrains the chemical diversity we can explore. Studies such as A. Y. Jaziri et al. (2025) have demonstrated that atmospheric metallicity can significantly affect the observable spectra and molecular abundances in sub-Neptune atmospheres, we have not systematically varied this parameter. Additionally, the C/O ratio plays a crucial role in determining atmospheric composition by affecting the chemical equilibrium partitioning between carbon and oxygen bearing species. C/O ratios above or below solar values can substantially alter the relative abundances of key molecules such as CH₄, H₂O, CO, and CO₂, which are primary observational molecules (N. Madhusudhan 2012). The interplay between metallicity, C/O ratio, and our explored parameters intrinsic temperature and vertical mixing likely creates a more complex parameter space than we have yet to investigate. Future work incorporating a grid of metallicity and C/O values would provide a more complete picture of the degeneracies and unique atmospheric signatures accessible through observations.

Our chemical network focuses on carbon, hydrogen, nitrogen, and oxygen (NCHO) species, excluding sulfur chemistry from our systematic parameter-grid exploration. While we verified that sulfur inclusion produces minimal differences in our benchmark models (1.8 ppm difference), sulfur-bearing species such as H₂S, SO₂, and other sulfur compounds can play important roles in exoplanet atmospheric chemistry and may exhibit distinct sensitivities to intrinsic temperature and vertical mixing that we have not systematically characterized. The recent detection and

modeling of sulfur species in exoplanet atmospheres, such as the analysis of GJ 436b by [S.-M. Tsai et al. \(2023\)](#), demonstrates the potential observational significance of these molecules for atmospheric characterization. Future work should extend our systematic parameter space exploration to include sulfur chemistry networks, particularly for planets where sulfur species may be observable with JWST and other next generation instruments.

We do not explicitly include aerosol and haze production, which are known to significantly affect transmission spectra by reducing molecular absorption features and steepening spectral trends across wavelength ([J. J. Fortney 2005](#); [D. K. Sing et al. 2016](#)). In extreme cases, thick photochemical hazes can completely mute spectral features, as observed in planets like GJ 1214b ([E. M.-R. Kempton et al. 2014](#)). While our intrinsic temperature variations account for some temperature-dependent processes, specifically water condensation and cold trapping, we do not model the full microphysical properties, vertical distributions, or compositional variations of condensate clouds for other molecular species, nor do we include photochemical hazes. However, our systematic exploration of intrinsic temperature effects provides insights into potential haze formation trends. Since photochemical hazes in sub-Neptune atmospheres are primarily produced from hydrocarbon precursors like CH₄ ([R. Hu et al. 2025](#)), our finding that higher intrinsic temperatures systematically deplete CH₄ abundances suggests an intriguing hypothesis: intrinsically hotter sub-Neptunes should exhibit clearer atmospheres due to reduced availability of haze precursors. This prediction could be tested observationally, as sub-Neptunes with evidence for heated interiors should show stronger molecular absorption features compared to their cooler counterparts. While a full exploration of the complex coupling between intrinsic temperature, atmospheric chemistry, and haze microphysics represents an important avenue for future work, the fundamental chemical trends we identify provide a framework for understanding how interior thermal states may influence observable atmospheric properties beyond gas-phase chemistry alone. For K2-18b specifically, the lack of substantial haze signatures in current observations ([N. Madhusudhan et al. 2023](#)) may be consistent with our inference of moderately heated interior conditions that deplete haze-forming precursors.

Photochemically active species such as NH₃ and CH₄ are particularly sensitive to the stellar UV environment, as photodissociation rates depend strongly on the stellar spectrum in the ultraviolet ([R. Hu et al. 2012](#); [J. I. Moses et al. 2011](#)). Different host stars exhibit distinct UV to visible flux ratios, which can lead to different photochemical pathways and molecular abundances ([A. Segura et al. 2005](#); [K. France et al. 2013](#); [Y. Kawashima & M. Ikoma 2019](#)). [G. J. Cooke & N. Madhusudhan \(2024\)](#) conducted a detailed exploration of K2-18's stellar spectrum and its photochemical implications for atmospheric modeling in their appendix, demonstrating the importance of accurate stellar characterization for sub-Neptune atmospheric chemistry. By restricting our analysis to a single stellar spectrum, we did not assess how variations in stellar characteristics affect the observability and abundance patterns of key atmospheric molecules in sub-Neptune atmospheres. Additionally, we do not account for stellar contamination effects in our transmission spectrum calculations. K2-18 exhibits higher activity than typical M dwarfs of its age due to observable star spots and activity cycles ([T. Barclay et al. 2021](#)), and such stellar contamination can introduce spectral features that mimic or mask atmospheric signatures ([B. V. Rackham et al. 2018, 2019](#)). The enhanced activity of K2-18 emphasizes the importance of obtaining detailed UV spectra for individual host stars rather than relying on proxy spectra, as stellar activity affects both the photochemical environment and observed transmission spectra.

5. CONCLUSION

We present the first comprehensive exploration of intrinsic temperature (T_{int}) vertical mixing (K_{zz}) parameter space for temperate sub-Neptune atmospheres (K2-18b analogs), spanning $T_{\text{int}} = 60\text{--}450$ K and $K_{zz} = 10^5\text{--}10^{12}$ cm² s⁻¹ using coupled PICASO and VULCAN models. Our systematic analysis reveals that these parameters, often treated as fixed in prior work, exert fundamental control over atmospheric composition and observable spectra.

1. Molecular abundance patterns exhibit distinct sensitivity regimes. CH₄ and NH₃ show strong temperature dependence with comparatively weaker sensitivity to mixing strength, consistent with thermochemical control. CO and H₂O display moderate coupling between thermal and dynamical effects, while HCN demonstrates extreme disequilibrium behavior, varying by up to 6 orders of magnitude across the explored K_{zz} range. CO₂ emerges as a diagnostic of intermediate thermal states, reaching peak abundances at $T_{\text{int}} = 200\text{--}350$ K under moderate mixing conditions.

2. Transmission spectra across $0.5\text{--}5\ \mu\text{m}$ reveal systematic evolution with intrinsic temperature. Cool models ($T_{\text{int}} < 150\ \text{K}$) produce excessive CH_4 absorption inconsistent with observations, while hot models ($T_{\text{int}} > 400\ \text{K}$) show strongly depleted CH_4 and spectra dominated by H_2O opacity. Critically, intermediate models ($T_{\text{int}} = 250\text{--}350\ \text{K}$) reproduce the K2-18b benchmark spectrum, demonstrating that moderate interior heating can explain the observed molecular patterns without invoking Hycean scenarios.
3. Quenching analysis demonstrates that observable atmospheric composition reflects deep interior chemistry transported upward through pressure-dependent mixing. Chemical timescales decrease from $10^6\ \text{s}$ at low temperatures to $10^4\ \text{s}$ at high temperatures, converging with mixing timescales at intermediate T_{int} to yield the molecular abundance ratios observed in temperate sub-Neptunes.
4. A key challenge for compositional interpretation is the degeneracy between gas-rich sub-Neptunes with hot interiors and Hycean worlds with shallow surfaces. Both scenarios can produce similar CH_4 depletion and CO_2 enhancement, but through fundamentally different mechanisms: deep quenching versus photochemical destruction without recycling. Our models provide a diagnostic framework using HCN detection, H_2O measurements, and NH_3 upper limits to distinguish these competing scenarios.
5. For K2-18b specifically, spectral matching constrains the intrinsic temperature to $T_{\text{int}} = 250\text{--}350\ \text{K}$, indicating either a moderately heated sub-Neptune interior or alternative thermal structures consistent with different planetary scenarios. The convergence of our intermediate-temperature models with observed spectral features demonstrates that systematic exploration of thermal and mixing parameter space is essential for robust atmospheric interpretation, as compositional degeneracies can lead to misclassification of planetary scenarios without comprehensive parameter studies.

These results fundamentally change approaches to sub-Neptune characterization by demonstrating that thermal and mixing parameters cannot be treated as fixed quantities. The substantial degeneracies we identify between different atmospheric models highlight that single parameter assumptions can lead to incorrect conclusions about planetary composition and habitability. For current JWST observations, this motivates prioritizing multi-molecule diagnostics over single species detections.

At the population level, our results reveal the complexity of inferring surface conditions from atmospheric observations alone. The systematic parameter dependencies we identify demonstrate that atmospheric composition reflects a complex interplay of interior thermal evolution, mixing processes, and surface conditions. This complexity suggests that robust characterization of sub-Neptune chemistry requires comprehensive parameter space exploration rather than relying on simplified atmospheric models with fixed assumptions.

Future work should extend this analysis to include aerosol and haze formation, systematic variations in atmospheric metallicity and C/O ratios, and quantify the impact of stellar UV/visible spectral diversity, thereby fully characterizing the multi-dimensional parameter space governing sub-Neptune atmospheric diversity. The diagnostic framework developed here provides a foundation for more sophisticated atmospheric interpretation methods essential for advancing our understanding of the most abundant class of planets in the Galaxy.

ACKNOWLEDGMENTS

This work was partially supported by funding from the Center for Exoplanets and Habitable Worlds. The Center for Exoplanets and Habitable Worlds is supported by the Pennsylvania State University and the Eberly College of Science. Neha Dushyantha Kumar acknowledges funding support from the Erickson Discovery Grant for Summer 2025, which enabled the comprehensive parameter space exploration presented in this work.

We thank Shang-Min Tsai for his invaluable assistance and guidance in implementing VULCAN for our sub-Neptune atmospheric modeling, and for his contributions to the photochemical network development that made this systematic parameter space exploration possible. We also thank Luis Welbanks for his insightful discussions on K2-18b atmospheric characterization and for his presentation at the American Astronomical Society 247th meeting, which provided valuable perspective that helped shape the goals and direction of this manuscript.

The authors of this work recognize the (i) Penn State Institute for Computational and Data Sciences (RRID:SCR_025154) for providing access to computational research infrastructure within the Roar Core Facility (RRID: SCR_026424) and (ii) NASA High-End Computing (HEC) Program through the NASA Center for Climate Simulation (NCCS) at Goddard Space Flight Center.

CIC acknowledges support by NASA Headquarters through an appointment to the NASA Postdoctoral Program at the Goddard Space Flight Center, administered by ORAU through a contract with NASA, and support from NASA under award number 80GSFC24M0006.

Software: PICASO (N. Batalha et al. 2022; S. Mukherjee et al. 2023), VULCAN (S.-M. Tsai et al. 2021) exoatlas (Z. K. Berta-Thompson et al. 2025), matplotlib (J. D. Hunter 2007), numpy (S. van der Walt et al. 2011), pandas (W. McKinney 2011),

REFERENCES

Barclay, T., Kostov, V. B., Colón, K. D., et al. 2021, AJ, 162, 300, doi: [10.3847/1538-3881/ac2824](https://doi.org/10.3847/1538-3881/ac2824)

Barstow, J. K., Aigrain, S., Irwin, P. G. J., & Sing, D. K. 2017, ApJ, 834, 50, doi: [10.3847/1538-4357/834/1/50](https://doi.org/10.3847/1538-4357/834/1/50)

Batalha, N., Rooney, C., Robbins Blanch, N., & MacDonald, R. 2022, natashabatalha/picaso: Release 2.3, v2.3.0 Zenodo, doi: [10.5281/zenodo.6419943](https://doi.org/10.5281/zenodo.6419943)

Batalha, N. E., Marley, M. S., Lewis, N. K., & Fortney, J. J. 2019, ApJ, 878, 70, doi: [10.3847/1538-4357/ab1b51](https://doi.org/10.3847/1538-4357/ab1b51)

Benneke, B., & Seager, S. 2013, ApJ, 778, 153, doi: [10.1088/0004-637X/778/2/153](https://doi.org/10.1088/0004-637X/778/2/153)

Benneke, B., Wong, I., Piaulet, C., et al. 2019, ApJL, 887, L14, doi: [10.3847/2041-8213/ab59dc](https://doi.org/10.3847/2041-8213/ab59dc)

Benneke, B., Roy, P.-A., Coulombe, L.-P., et al. 2024, arXiv e-prints, arXiv:2403.03325, doi: [10.48550/arXiv.2403.03325](https://doi.org/10.48550/arXiv.2403.03325)

Berta-Thompson, Z. K., Wachiraphan, P., Stephens, A., et al. 2025, arXiv e-prints, arXiv:2507.02210, doi: [10.48550/arXiv.2507.02210](https://doi.org/10.48550/arXiv.2507.02210)

Christiansen, J. L., McElroy, D. L., Harbut, M., et al. 2025, PSJ, 6, 186, doi: [10.3847/PSJ/ade3c2](https://doi.org/10.3847/PSJ/ade3c2)

Cooke, G. J., & Madhusudhan, N. 2024, ApJ, 977, 209, doi: [10.3847/1538-4357/ad8cda](https://doi.org/10.3847/1538-4357/ad8cda)

Crossfield, I. J. M., Ahrer, E.-M., Brande, J., et al. 2025, ApJ, 994, 184, doi: [10.3847/1538-4357/ae17cb](https://doi.org/10.3847/1538-4357/ae17cb)

de Wit, J., Seager, S., & Niraula, P. 2025, arXiv e-prints, arXiv:2509.25323, doi: [10.48550/arXiv.2509.25323](https://doi.org/10.48550/arXiv.2509.25323)

Deming, L. D., & Seager, S. 2017, Journal of Geophysical Research (Planets), 122, 53, doi: [10.1002/2016JE005155](https://doi.org/10.1002/2016JE005155)

Espinoza, N., & Perrin, M. D. 2025, arXiv e-prints, arXiv:2505.20520, doi: [10.48550/arXiv.2505.20520](https://doi.org/10.48550/arXiv.2505.20520)

Fortney, J. J. 2005, MNRAS, 364, 649, doi: [10.1111/j.1365-2966.2005.09587.x](https://doi.org/10.1111/j.1365-2966.2005.09587.x)

Fortney, J. J. 2018, arXiv e-prints, arXiv:1804.08149, doi: [10.48550/arXiv.1804.08149](https://doi.org/10.48550/arXiv.1804.08149)

Fortney, J. J., Ikoma, M., Nettelmann, N., Guillot, T., & Marley, M. S. 2011, ApJ, 729, 32, doi: [10.1088/0004-637X/729/1/32](https://doi.org/10.1088/0004-637X/729/1/32)

Fortney, J. J., Visscher, C., Marley, M. S., et al. 2020, AJ, 160, 288, doi: [10.3847/1538-3881/abc5bd](https://doi.org/10.3847/1538-3881/abc5bd)

France, K., Froning, C. S., Linsky, J. L., et al. 2013, ApJ, 763, 149, doi: [10.1088/0004-637X/763/2/149](https://doi.org/10.1088/0004-637X/763/2/149)

Fulton, B. J., & Petigura, E. A. 2018, AJ, 156, 264, doi: [10.3847/1538-3881/aae828](https://doi.org/10.3847/1538-3881/aae828)

Fulton, B. J., Petigura, E. A., Howard, A. W., et al. 2017, AJ, 154, 109, doi: [10.3847/1538-3881/aa80eb](https://doi.org/10.3847/1538-3881/aa80eb)

Gardner, J. P., Mather, J. C., Clampin, M., et al. 2006, SSRV, 123, 485, doi: [10.1007/s11214-006-8315-7](https://doi.org/10.1007/s11214-006-8315-7)

Guillot, T. 2010, A&A, 520, A27, doi: [10.1051/0004-6361/200913396](https://doi.org/10.1051/0004-6361/200913396)

Guillot, T., & Gautier, D. 2015, in Treatise on Geophysics, ed. G. Schubert, 529–557, doi: [10.1016/B978-0-444-53802-4.00176-7](https://doi.org/10.1016/B978-0-444-53802-4.00176-7)

Heng, K., & Tsai, S.-M. 2016, ApJ, 829, 104, doi: [10.3847/0004-637X/829/2/104](https://doi.org/10.3847/0004-637X/829/2/104)

Howe, A. R., Burrows, A., & Deming, D. 2017, ApJ, 835, 96, doi: [10.3847/1538-4357/835/1/96](https://doi.org/10.3847/1538-4357/835/1/96)

Hsu, D. C., Ford, E. B., Ragozzine, D., & Ashby, K. 2019, AJ, 158, 109, doi: [10.3847/1538-3881/ab31ab](https://doi.org/10.3847/1538-3881/ab31ab)

Hu, R. 2021, ApJ, 921, 27, doi: [10.3847/1538-4357/ac1789](https://doi.org/10.3847/1538-4357/ac1789)

Hu, R., Seager, S., & Bains, W. 2012, ApJ, 761, 166, doi: [10.1088/0004-637X/761/2/166](https://doi.org/10.1088/0004-637X/761/2/166)

Hu, R., Bello-Arufe, A., Tokadjian, A., et al. 2025, arXiv e-prints, arXiv:2507.12622, doi: [10.48550/arXiv.2507.12622](https://doi.org/10.48550/arXiv.2507.12622)

Huang, Z., Yu, X., Tsai, S.-M., et al. 2024, ApJ, 975, 146, doi: [10.3847/1538-4357/ad76ac](https://doi.org/10.3847/1538-4357/ad76ac)

Hunter, J. D. 2007, Computing in Science & Engineering, 9, 90, doi: [10.1109/MCSE.2007.55](https://doi.org/10.1109/MCSE.2007.55)

Husser, T.-O., Wende-von Berg, S., Dreizler, S., et al. 2013, A&A, 553, A6, doi: [10.1051/0004-6361/201219058](https://doi.org/10.1051/0004-6361/201219058)

Innes, H., Tsai, S.-M., & Pierrehumbert, R. T. 2023, ApJ, 953, 168, doi: [10.3847/1538-4357/ace346](https://doi.org/10.3847/1538-4357/ace346)

Jaziri, A. Y., Sohier, O., Venot, O., & Carrasco, N. 2025, arXiv e-prints, arXiv:2507.14983, doi: [10.48550/arXiv.2507.14983](https://doi.org/10.48550/arXiv.2507.14983)

Kawashima, Y., & Ikoma, M. 2019, ApJ, 877, 109, doi: [10.3847/1538-4357/ab1b1d](https://doi.org/10.3847/1538-4357/ab1b1d)

Kempton, E. M.-R., Perna, R., & Heng, K. 2014, ApJ, 795, 24, doi: [10.1088/0004-637X/795/1/24](https://doi.org/10.1088/0004-637X/795/1/24)

Kreidberg, L. 2018, in *Handbook of Exoplanets*, ed. H. J. Deeg & J. A. Belmonte, 100, doi: [10.1007/978-3-319-55333-7_100](https://doi.org/10.1007/978-3-319-55333-7_100)

Lammer, H., Zerkle, A. L., Gebauer, S., et al. 2018, A&A Rv, 26, 2, doi: [10.1007/s00159-018-0108-y](https://doi.org/10.1007/s00159-018-0108-y)

Leconte, J., Wu, H., Menou, K., & Murray, N. 2015, Science, 347, 632, doi: [10.1126/science.1258686](https://doi.org/10.1126/science.1258686)

Li, J., Bergin, E. A., Hirschmann, M. M., et al. 2025, Soot Planets instead of Water Worlds, <https://arxiv.org/abs/2508.16781>

Lopez, E. D., & Fortney, J. J. 2014, ApJ, 792, 1, doi: [10.1088/0004-637X/792/1/1](https://doi.org/10.1088/0004-637X/792/1/1)

Lupu, R., Freedman, R., Gharib-Nezhad, E., Visscher, C., & Molliere, P. 2021, Correlated k coefficients for H2-He atmospheres: 196 spectral windows and 1460 pressure-temperature points, Zenodo, doi: [10.5281/zenodo.7542068](https://doi.org/10.5281/zenodo.7542068)

Madhusudhan, N. 2012, ApJ, 758, 36, doi: [10.1088/0004-637X/758/1/36](https://doi.org/10.1088/0004-637X/758/1/36)

Madhusudhan, N., Nixon, M. C., Welbanks, L., Piette, A. A., & Booth, R. A. 2020, ApJL, 891, L7, doi: [10.3847/2041-8213/ab7229](https://doi.org/10.3847/2041-8213/ab7229)

Madhusudhan, N., Piette, A. A. A., & Constantinou, S. 2021, ApJ, 918, 1, doi: [10.3847/1538-4357/abfd9c](https://doi.org/10.3847/1538-4357/abfd9c)

Madhusudhan, N., Sarkar, S., Constantinou, S., et al. 2023, ApJL, 956, L13, doi: [10.3847/2041-8213/acf577](https://doi.org/10.3847/2041-8213/acf577)

Madhusudhan, N., & Seager, S. 2009, ApJ, 707, 24, doi: [10.1088/0004-637X/707/1/24](https://doi.org/10.1088/0004-637X/707/1/24)

Marley, M. S., Saumon, D., Visscher, C., et al. 2021, ApJ, 920, 85, doi: [10.3847/1538-4357/ac141d](https://doi.org/10.3847/1538-4357/ac141d)

Mckinney, W. 2011, Python High Performance Science Computer

Millholland, S. 2019, ApJ, 886, 72, doi: [10.3847/1538-4357/ab4c3f](https://doi.org/10.3847/1538-4357/ab4c3f)

Millholland, S., Petigura, E., & Batygin, K. 2020, ApJ, 897, 7, doi: [10.3847/1538-4357/ab959c](https://doi.org/10.3847/1538-4357/ab959c)

Mitchell, E. G., & Madhusudhan, N. 2025, MNRAS, 538, 1653, doi: [10.1093/mnras/staf094](https://doi.org/10.1093/mnras/staf094)

Montet, B. T., Morton, T. D., Foreman-Mackey, D., et al. 2015, ApJ, 809, 25, doi: [10.1088/0004-637X/809/1/25](https://doi.org/10.1088/0004-637X/809/1/25)

Moses, J. I., Visscher, C., Fortney, J. J., et al. 2011, ApJ, 737, 15, doi: [10.1088/0004-637X/737/1/15](https://doi.org/10.1088/0004-637X/737/1/15)

Mukherjee, S., Batalha, N. E., Fortney, J. J., & Marley, M. S. 2023, ApJ, 942, 71, doi: [10.3847/1538-4357/ac9f48](https://doi.org/10.3847/1538-4357/ac9f48)

Mukherjee, S., Fortney, J. J., Wogan, N. F., Sing, D. K., & Ohno, K. 2025, ApJ, 985, 209, doi: [10.3847/1538-4357/adc7b3](https://doi.org/10.3847/1538-4357/adc7b3)

Öberg, K. I., Murray-Clay, R., & Bergin, E. A. 2011, ApJL, 743, L16, doi: [10.1088/2041-8205/743/1/L16](https://doi.org/10.1088/2041-8205/743/1/L16)

Parmentier, V., Showman, A. P., & Lian, Y. 2013, A&A, 558, A91, doi: [10.1051/0004-6361/201321132](https://doi.org/10.1051/0004-6361/201321132)

Rackham, B. V., Apai, D., & Giampapa, M. S. 2018, ApJ, 853, 122, doi: [10.3847/1538-4357/aaa08c](https://doi.org/10.3847/1538-4357/aaa08c)

Rackham, B. V., Apai, D., & Giampapa, M. S. 2019, AJ, 157, 96, doi: [10.3847/1538-3881/aaf892](https://doi.org/10.3847/1538-3881/aaf892)

Rimmer, P. B., Ferus, M., Waldmann, I. P., et al. 2020, ApJ, 888, 21, doi: [10.3847/1538-4357/ab55e8](https://doi.org/10.3847/1538-4357/ab55e8)

Rogers, L. A. 2015, ApJ, 801, 41, doi: [10.1088/0004-637X/801/1/41](https://doi.org/10.1088/0004-637X/801/1/41)

Rogers, L. A., & Seager, S. 2010a, ApJ, 716, 1208, doi: [10.1088/0004-637X/716/2/1208](https://doi.org/10.1088/0004-637X/716/2/1208)

Rogers, L. A., & Seager, S. 2010b, ApJ, 712, 974, doi: [10.1088/0004-637X/712/2/974](https://doi.org/10.1088/0004-637X/712/2/974)

Roman, M., & Rauscher, E. 2019, ApJ, 872, 1, doi: [10.3847/1538-4357/aafdb5](https://doi.org/10.3847/1538-4357/aafdb5)

Sarkis, P., Henning, T., Kürster, M., et al. 2018, AJ, 155, 257, doi: [10.3847/1538-3881/aac108](https://doi.org/10.3847/1538-3881/aac108)

Segura, A., Kasting, J. F., Meadows, V., et al. 2005, Astrobiology, 5, 706, doi: [10.1089/ast.2005.5.706](https://doi.org/10.1089/ast.2005.5.706)

Shorttle, O., Jordan, S., Nicholls, H., Lichtenberg, T., & Bower, D. J. 2024, ApJL, 962, L8, doi: [10.3847/2041-8213/ad206e](https://doi.org/10.3847/2041-8213/ad206e)

Sing, D. K., Fortney, J. J., Nikolov, N., et al. 2016, Nature, 529, 59, doi: [10.1038/nature16068](https://doi.org/10.1038/nature16068)

Sing, D. K., Rustamkulov, Z., Thorngren, D. P., et al. 2024, Nature, 630, 831, doi: [10.1038/s41586-024-07395-z](https://doi.org/10.1038/s41586-024-07395-z)

Soni, V., & Acharyya, K. 2024, ApJ, 977, 52, doi: [10.3847/1538-4357/ad891f](https://doi.org/10.3847/1538-4357/ad891f)

Stassun, K. G., Oelkers, R. J., Paegert, M., et al. 2019, AJ, 158, 138, doi: [10.3847/1538-3881/ab3467](https://doi.org/10.3847/1538-3881/ab3467)

Steinrueck, M. E., Koskinen, T., Lavvas, P., et al. 2023, ApJ, 951, 117, doi: [10.3847/1538-4357/acd4bb](https://doi.org/10.3847/1538-4357/acd4bb)

Thorngren, D., Gao, P., & Fortney, J. J. 2019, ApJL, 884, L6, doi: [10.3847/2041-8213/ab43d0](https://doi.org/10.3847/2041-8213/ab43d0)

Tsai, S.-M., Innes, H., Wogan, N. F., & Schwierman, E. W. 2024, ApJL, 966, L24, doi: [10.3847/2041-8213/ad3801](https://doi.org/10.3847/2041-8213/ad3801)

Tsai, S.-M., Malik, M., Kitzmann, D., et al. 2021, ApJ, 923, 264, doi: [10.3847/1538-4357/ac29bc](https://doi.org/10.3847/1538-4357/ac29bc)

Tsai, S.-M., Lee, E. K. H., Powell, D., et al. 2023, *Nature*, 617, 483, doi: [10.1038/s41586-023-05902-2](https://doi.org/10.1038/s41586-023-05902-2)

van der Walt, S., Colbert, S. C., & Varoquaux, G. 2011, *Computing in Science & Engineering*, 13, 22, doi: [10.1109/MCSE.2011.37](https://doi.org/10.1109/MCSE.2011.37)

Visscher, C., Lodders, K., & Fegley, Jr., B. 2006, *ApJ*, 648, 1181, doi: [10.1086/506245](https://doi.org/10.1086/506245)

Visscher, C., Lodders, K., & Fegley, Jr., B. 2010, *ApJ*, 716, 1060, doi: [10.1088/0004-637X/716/2/1060](https://doi.org/10.1088/0004-637X/716/2/1060)

Visscher, C., & Moses, J. I. 2011, *ApJ*, 738, 72, doi: [10.1088/0004-637X/738/1/72](https://doi.org/10.1088/0004-637X/738/1/72)

Welbanks, L., Bell, T. J., Beatty, T. G., et al. 2024, *Nature*, 630, 836, doi: [10.1038/s41586-024-07514-w](https://doi.org/10.1038/s41586-024-07514-w)

Wogan, N. F., Batalha, N. E., Zahnle, K. J., et al. 2024, *ApJL*, 963, L7, doi: [10.3847/2041-8213/ad2616](https://doi.org/10.3847/2041-8213/ad2616)

Wogan, N. F., Batalha, N. E., Zahnle, K., et al. 2025, arXiv e-prints, arXiv:2509.25578, doi: [10.48550/arXiv.2509.25578](https://doi.org/10.48550/arXiv.2509.25578)

Wolfgang, A., Rogers, L. A., & Ford, E. B. 2016, *ApJ*, 825, 19, doi: [10.3847/0004-637X/825/1/19](https://doi.org/10.3847/0004-637X/825/1/19)

Yu, X., Moses, J. I., Fortney, J. J., & Zhang, X. 2021, *ApJ*, 914, 38, doi: [10.3847/1538-4357/abfdc7](https://doi.org/10.3847/1538-4357/abfdc7)

Zahnle, K., Marley, M. S., Freedman, R. S., Lodders, K., & Fortney, J. J. 2009, *ApJL*, 701, L20, doi: [10.1088/0004-637X/701/1/L20](https://doi.org/10.1088/0004-637X/701/1/L20)

Zamyatina, M., Christie, D. A., Hébrard, E., et al. 2024, *MNRAS*, 529, 1776, doi: [10.1093/mnras/stae600](https://doi.org/10.1093/mnras/stae600)

Zeng, L., & Seager, S. 2008, *PASP*, 120, 983, doi: [10.1086/591807](https://doi.org/10.1086/591807)

Zeng, L., Jacobsen, S. B., Sasselov, D. D., et al. 2019, *Proceedings of the National Academy of Science*, 116, 9723, doi: [10.1073/pnas.1812905116](https://doi.org/10.1073/pnas.1812905116)

Zhang, X., & Showman, A. P. 2018, *ApJ*, 866, 1, doi: [10.3847/1538-4357/aada85](https://doi.org/10.3847/1538-4357/aada85)

APPENDIX

Table A1 summarizes the molecular abundance ranges from our systematic parameter-space exploration, providing a reference for the chemical diversity across different thermal and dynamical regimes in K2-18b analog atmospheres. These abundance ranges, derived from our coupled PICASO–VULCAN modeling grid (Figures 3 and 4), can inform atmospheric retrievals, guide observational strategies, and facilitate model comparisons. The temperature-regime classifications reflect distinct chemical behaviors identified in Section 3, while mixing dependencies highlight species-specific sensitivities that serve as atmospheric dynamics diagnostics. Values represent photospheric means accounting for coupled thermochemical, transport, and photochemical processes across our full parameter space.

Molecule	Temperature Regime	Mixing Conditions	Abundance Range	\log_{10} Abundance
CH₄ (Methane)	Cool (< 150 K)	All K_{zz} (10^5 – 10^{12} cm 2 s $^{-1}$)	10^{-3} to 10^{-2}	–3 to –2
	Intermediate (200–350 K)	All K_{zz} (10^5 – 10^{12} cm 2 s $^{-1}$)	10^{-4} to 10^{-3}	–4 to –3
	Hot (> 400 K)	All K_{zz} (10^5 – 10^{12} cm 2 s $^{-1}$)	10^{-6} to 10^{-5}	–6 to –5
NH₃ (Ammonia)	Cool (< 150 K)	All K_{zz} (10^5 – 10^{12} cm 2 s $^{-1}$)	10^{-3} to $10^{-2.5}$	–3 to –2.5
	Intermediate (200–350 K)	All K_{zz} (10^5 – 10^{12} cm 2 s $^{-1}$)	10^{-4} to 10^{-3}	–4 to –3
	Hot (> 400 K)	All K_{zz} (10^5 – 10^{12} cm 2 s $^{-1}$)	$10^{-5.5}$	–5.5
CO (Carbon Monoxide)	Cool (< 150 K)	Low K_{zz} (10^5 – 10^8 cm 2 s $^{-1}$)	10^{-3} to 10^{-2}	–3 to –2
	Cool (< 150 K)	High K_{zz} (10^{10} – 10^{12} cm 2 s $^{-1}$)	10^{-2} to $10^{-1.5}$	–2 to –1.5
	Intermediate (200–350 K)	All K_{zz} (10^5 – 10^{12} cm 2 s $^{-1}$)	$10^{-1.5}$ to 10^{-1}	–1.5 to –1
	Hot (> 400 K)	All K_{zz} (10^5 – 10^{12} cm 2 s $^{-1}$)	10^{-1}	–1
CO₂ (Carbon Dioxide)	Cool (< 150 K)	All K_{zz} (10^5 – 10^{12} cm 2 s $^{-1}$)	$10^{-4.5}$ to $10^{-3.5}$	–4.5 to –3.5
	Intermediate (200–350 K)	Low K_{zz} (10^5 – 10^8 cm 2 s $^{-1}$)	$10^{-2.5}$ to 10^{-2}	–2.5 to –2
	Intermediate (200–350 K)	High K_{zz} (10^{10} – 10^{12} cm 2 s $^{-1}$)	10^{-2} to $10^{-1.5}$	–2 to –1.5
	Hot (> 400 K)	All K_{zz} (10^5 – 10^{12} cm 2 s $^{-1}$)	$10^{-4.5}$ to $10^{-3.5}$	–4.5 to –3.5
H₂O (Water)	Cool (< 150 K)	All K_{zz} (10^5 – 10^{12} cm 2 s $^{-1}$)	10^{-3} to $10^{-2.5}$	–3 to –2.5
	Intermediate (200–350 K)	All K_{zz} (10^5 – 10^{12} cm 2 s $^{-1}$)	$10^{-1.5}$ to 10^{-1}	–1.5 to –1
	Hot (> 400 K)	All K_{zz} (10^5 – 10^{12} cm 2 s $^{-1}$)	10^{-1} to $10^{-0.5}$	–1 to –0.5
HCN (Hydrogen Cyanide)	Cool (< 150 K)	All K_{zz} (10^5 – 10^{12} cm 2 s $^{-1}$)	$10^{-8.5}$ to 10^{-8}	–8.5 to –8
	Intermediate (200–350 K)	Low K_{zz} (10^5 – 10^8 cm 2 s $^{-1}$)	10^{-7} to 10^{-6}	–7 to –6
	Intermediate (200–350 K)	High K_{zz} ($> 10^{10}$ cm 2 s $^{-1}$)	$10^{-8.5}$ to 10^{-8}	–8.5 to –8
	Hot (> 400 K)	Low K_{zz} (10^5 cm 2 s $^{-1}$)	$10^{-5.5}$ to 10^{-5}	–5.5 to –5
	Hot (> 400 K)	High K_{zz} ($> 10^{10}$ cm 2 s $^{-1}$)	$10^{-8.5}$ to 10^{-8}	–8.5 to –8

Table A1. Molecular abundance ranges in K2-18b analog atmospheres. Mean molecular abundances (volume mixing ratios) in the photospheric region (10^{-3} – 10^{-4} bar) as a function of intrinsic temperature and vertical mixing strength. Results from coupled PICASO–VULCAN atmospheric models spanning $T_{int} = 60$ – 500 K and $K_{zz} = 10^5$ – 10^{12} cm 2 s $^{-1}$. Temperature regimes: cool (< 150 K), intermediate (200–350 K), and high (> 400 K).

Figure A1 demonstrates the robustness of our atmospheric modeling approach through two key validation tests. First, we benchmark our PICASO–VULCAN framework against the established N. F. Wogan et al. (2024) mini-Neptune model for K2-18b, showing excellent agreement across most wavelengths with differences typically below observational precision. The largest systematic offset occurs in the 2.5–3.0 μ m region (~ 15.7 ppm). Second, we validate our decision to use the simplified NCHO chemical network by comparing against the full SNCHO network, finding negligible differences (1.2 ± 0.5 ppm wavelength-averaged) that confirm sulfur chemistry does not significantly impact our primary diagnostic molecules. While this validation supports our current approach, future work should systematically explore the full parameter grid using the SNCHO chemical network to comprehensively assess potential sulfur chemistry effects across the complete range of intrinsic temperatures and vertical mixing coefficients. These validation tests support

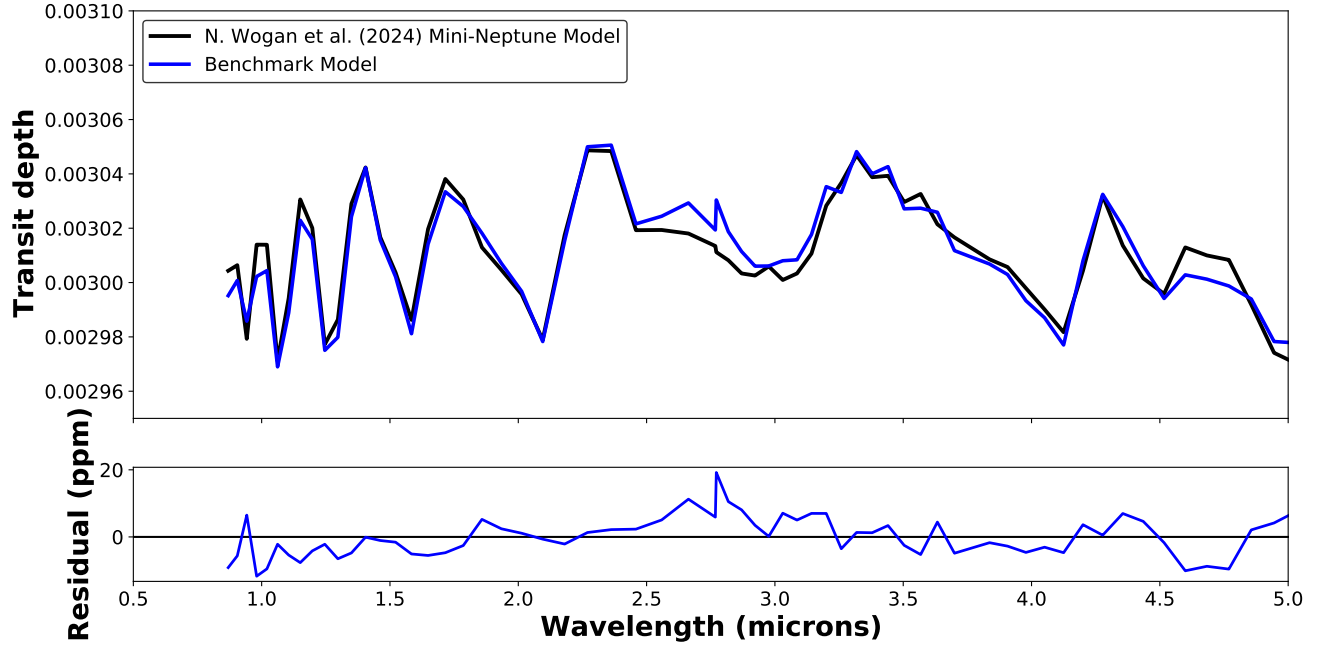
the reliability of our systematic parameter space exploration and strengthen confidence in our conclusions about the role of intrinsic temperature and vertical mixing in sub-Neptune atmospheric composition.

Table A2 quantifies the critical timescales and pressure levels governing disequilibrium chemistry in K2-18b analog atmospheres, providing diagnostics for how interior thermal states and atmospheric mixing determine observable molecular abundances (C. Visscher et al. 2006, 2010; J. I. Moses et al. 2011). These quenching parameters define transition points where rapid vertical transport freezes deep atmospheric compositions that are transported to the observable photosphere (C. Visscher et al. 2010). The systematic variation of chemical timescales with K_{zz} and temperature reveals the physical mechanisms underlying our abundance trends (Table A1) and explains why different molecules exhibit distinct thermal and dynamical sensitivities (J. I. Moses et al. 2011; R. Hu 2021). Comparison between variable and constant K_{zz} profiles demonstrates that altitude-dependent mixing creates more complex quenching behavior than simple parameterizations (N. F. Wogan et al. 2024), highlighting the importance of realistic transport modeling for accurate atmospheric predictions

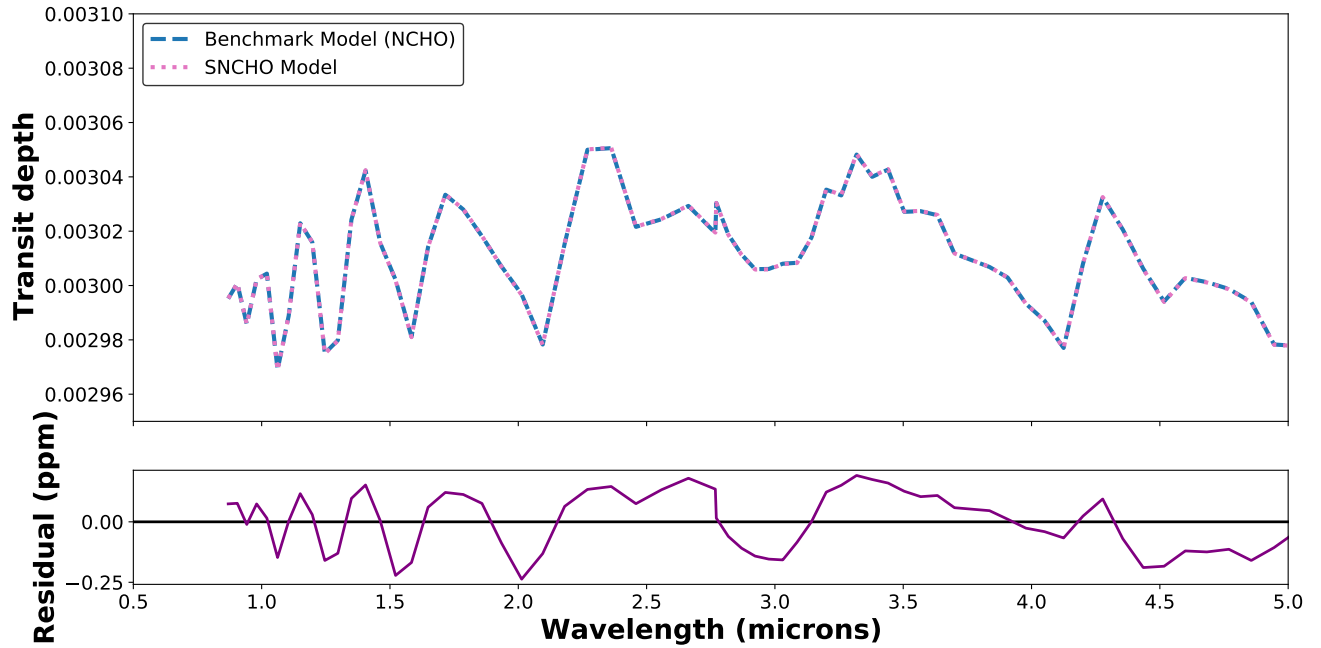
(a) Methane (CH₄)(b) Ammonia (NH₃)

K_{zz} (cm ² s ⁻¹)	T_q (K)	P_q range (bar)	τ_{chem} (s)	K_{zz} (cm ² s ⁻¹)	T_q (K)	P_q range (bar)	τ_{chem} (s)
Variable K_{zz}				Variable K_{zz}			
1 × 10 ⁵	60	10 ¹ –10 ²	123 ± 921	1 × 10 ⁵	60	10 ²	100.0 ± 746.3
1 × 10 ⁵	250	10 ⁰ –10 ¹	2142 ± 15996	1 × 10 ⁵	250	10 ¹	1735 ± 12957
5.6 × 10 ⁶	450	10 ⁻¹ –10 ⁰	149 ± 1115	1 × 10 ⁵	450	10 ⁰ –10 ⁻¹	5622 ± 41979
Constant K_{zz}				Constant K_{zz}			
1 × 10 ⁵	60	10 ¹ –10 ²	1.5 ± 11.1	1 × 10 ⁵	60	10 ²	1.2 ± 9.0
1 × 10 ⁵	250	10 ⁰ –10 ¹	25.9 ± 193.5	1 × 10 ⁵	250	10 ¹	21.0 ± 156.8
1 × 10 ⁵	450	10 ⁻¹ –10 ⁰	84.0 ± 627.1	1 × 10 ⁵	450	10 ⁰ –10 ⁻¹	68.0 ± 507.9
1 × 10 ⁸	60	10 ¹ –10 ²	0.242 ± 1.806	1 × 10 ⁸	60	10 ²	0.196 ± 1.463
1 × 10 ⁸	250	10 ⁰ –10 ¹	4.2 ± 31.4	1 × 10 ⁸	250	10 ¹	3.4 ± 25.4
1 × 10 ⁸	450	10 ⁻¹ –10 ⁰	13.6 ± 101.6	1 × 10 ⁸	450	10 ⁰ –10 ⁻¹	11.0 ± 82.3
1 × 10 ¹⁰	60	10 ² –10 ^{2.5}	0.024 ± 0.181	1 × 10 ¹⁰	60	10 ²	0.020 ± 0.146
1 × 10 ¹⁰	250	10 ¹ –10 ^{1.5}	0.420 ± 3.135	1 × 10 ¹⁰	250	10 ¹	0.340 ± 2.539
1 × 10 ¹⁰	450	10 ⁰ –10 ¹	1.4 ± 10.2	1 × 10 ¹⁰	450	10 ¹	1.1 ± 8.2
1 × 10 ¹²	60	10 ² –10 ^{2.5}	(4.0 ± 29.9) × 10 ⁻³	1 × 10 ¹²	60	10 ²	(3.2 ± 24.2) × 10 ⁻³
1 × 10 ¹²	250	10 ¹ –10 ²	0.069 ± 0.518	1 × 10 ¹²	250	10 ¹	0.056 ± 0.420
1 × 10 ¹²	450	10 ⁰ –10 ¹	0.225 ± 1.679	1 × 10 ¹²	450	10 ¹	0.182 ± 1.360

Table A2. Quenching timescales for CH₄ and NH₃ as a function of vertical eddy diffusion coefficient (K_{zz}). Quench pressure indicates the atmospheric level where chemical and mixing timescales become equal ($\tau_{\text{chem}} = \tau_{\text{mix}}$).



(a) N. Wogan et al. (2024) Mini-Neptune Model vs. Benchmark Model



(b) Benchmark vs. SNCHO Model

Figure A1. Comparison plots for K2-18b model spectra. Panel (a) shows the transmission spectrum comparison between the N. Wogan et al. (2024) Mini-Neptune Model (black line) and our Benchmark Model (blue line) across wavelengths from 0.5–5.0 μm , with residuals plotted below showing differences typically < 10 ppm except in the 2.5–3.0 μm region. Panel (b) shows the comparison between the Benchmark model (blue dashed line) and our SNCHO model (pink dotted line), demonstrating the minimal impact of sulfur chemistry inclusion on the primary spectral features. The excellent agreement validates our PICASO-VULCAN modeling framework, with wavelength-averaged differences of 1.2 ± 0.5 ppm between NCHO and SNCHO models, confirming that sulfur chemistry exclusion does not introduce systematic biases in our key diagnostic species (CH_4 , CO_2 , H_2O , NH_3).